
Article:
Lu, X., Xie, P. orcid.org/0000-0001-7156-7061, Ingham, D.B. et al. (2 more authors) (2019) Modelling of CO2 absorption in a rotating packed bed using an Eulerian porous media approach. Chemical Engineering Science, 199. pp. 302-318. ISSN 0009-2509

https://doi.org/10.1016/j.ces.2019.01.029

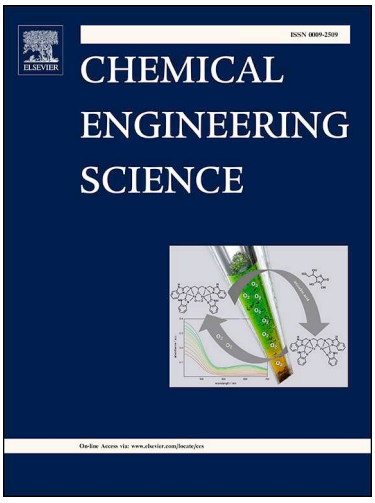

Modelling of CO_2 absorption in a rotating packed bed using an Eulerian porous media approach

X. Lu, P. Xie, D.B. Ingham, L. Ma, M. Pourkashanian

PII: S0009-2509(19)30109-5
DOI: https://doi.org/10.1016/j.ces.2019.01.029
Reference: CES 14743

To appear in: *Chemical Engineering Science*

Received Date: 30 October 2018
Revised Date: 20 December 2018
Accepted Date: 22 January 2019

Please cite this article as: X. Lu, P. Xie, D.B. Ingham, L. Ma, M. Pourkashanian, Modelling of CO_2 absorption in a rotating packed bed using an Eulerian porous media approach, *Chemical Engineering Science* (2019), doi: https://doi.org/10.1016/j.ces.2019.01.029

Modelling of CO_2 absorption in a rotating packed bed using an Eulerian porous media approach

X. Lu, P. Xie, D.B. Ingham, L. Ma*, M. Pourkashanian

Energy 2050, Department of Mechanical Engineering, Faculty of Engineering, University of Sheffield, Sheffield S10 2TN UK

*Corresponding author.

Email address: lin.ma@sheffield.ac.uk (L. Ma)

Highlights

- Application of a new porous media model for the gas-liquid flow in a RPB.
- Closure model of the interfacial area derived from the VOF simulation.
- Successful Eulerian simulation of CO_2 absorption by liquid amine in a lab-scale RPB.

Abstract

The rotating packed bed (RPB) is a promising reactor for CO_2 capture with liquid amine because of its high mass transfer rate and energy and space savings. The CFD simulations of RPBs generally use the volume of fluid (VOF) method, but this method is prohibitively expensive for 3D simulations, in particular for large-scale reactors. The Eulerian method is a promising and effective method; however, there are still several difficulties, such as the settings for the porous media models in the gas-liquid counter-current flow and the interfacial area between the gas and liquid. To overcome these difficulties in the Eulerian method, this paper uses a new porous media model, a novel liquid generation-elimination model for numerically investigating the gas-liquid counter-current flow in RPBs and a new interfacial area model derived from the VOF simulation. These new models, incorporating the two-film reaction-enhancement mass transfer model, have successfully simulated the CO_2 capture process with monoethanolamine (MEA) solutions in a RPB under both low (30 wt%) and high (90 wt%) concentrations conditions. The results show that the overall gas phase mass transfer coefficient (K_Ga) increases with increasing the rotation speeds and the liquid to gas mass flow rate (L/G ratio). The simulations were validated by the experimental data and the results were analysed and discussed.

Key words: Rotating packed bed, CFD simulation, CO_2 absorption, Liquid amine, and Porous media model

1. Introduction

CO_2 is one of the dominate greenhouse gases and contributes more than 60% to the global warming (Halmann and Stenberg et al., 1999). In 2015, among all CO_2 emissions from human activities, about 41% comes from coal combustion (Shearer et al., 2017) and the coal for electricity generation occupies 73% of all the coal consumption in 2015 (U.S. EIA, 2017). Therefore, the total power plants in the world contribute up to 30% of the total CO_2 emissions. Although the restrictions on the utilization of coal has been carried out, the electricity from coal combustion still dominates in the world and it contributes about 40% of the electricity generated from coal combustion (IEA, 2017) and many coal-fired stations are replaced with gas fired power stations. Therefore, the purification and storage of CO_2 from the fossil fuel combustion power plants is still a current urgent issue.

The absorption and desorption of CO_2 in the post combustion process generally uses liquid amine as the sorbents and this method is reasonably mature in comparison with other methods, such as solid amine and metal organic frameworks (MOFs). For this process, the traditional packed bed (PB) is commonly used, including randomly packed beds and structured packed beds and some large demonstration PB facilities have been constructed in some countries, such as at FerryBridge in the UK, Plant Barry in the USA or at Shidongkou in China. In 2014, SaskPower built the world first commercialized power station that successfully uses carbon capture and storage technology in Estevan, Saskatchewan, Canada. The absorber for the carbon capture is 20 meters long and 12 meters in diameter and the carbon capture facility is capable of capturing up to 1.3 million tons of CO_2 per year (Saskpower, 2017). The total CO_2 capture efficiency reaches up to 90% but the investment for the construction of this plant costed up to 1.3 billion US dollars (Oko et al., 2017). The gigantic solvent scrubbers occupy a very large space and high buildings are required to install them. The operation of this facility needs to pump large amounts of liquid absorbent to the

top of the absorber, therefore high energy costs are involved. In addition to the traditional PBs, the hollow fiber membrane contactor (HFMC) is another promising, efficient and flexible reactor for CO_2 absorption by liquid amine, but the commercial utilization has been impeded because of the huge expenditure on membranes for the processing of gigantic amounts of CO_2 from the power plant and the current membrane still has low permeability, low separation factors and low in withstanding high temperatures (Mansourizadeh and Ismail, 2009).

A recently developed process intensified reactor, namely the rotating packed bed (RPB), is more promising for the application in CO_2 absorption and desorption and this is because it demonstrates that the RPB could save reactor size and energy, and it has a high efficient operation. Under the same process conditions, the RPB has about 9.7 times reactor volume reduction compared to the conventional PB (Joel et al., 2017). Further, the total gas phase mass transfer coefficient for the RPB is about 1.2 times that for the traditional PB (Jassim et al., 2007; Kang et al., 2016). Nowadays, the research on CO_2 capture in RPBs has been carried out at several establishments, institutes and universities in the world (Zhao et al., 2016; Wang et al., 2015).

In reality, the RPB is a special PB, which is operated under a rotating field, and the characteristics of the gas and liquid flow have some similarities with those in the traditional PB but have a higher gravity force. The operation of CO_2 absorption in the traditional PB is that a CO_2 lean amine solution enters the top of the absorber and the flue gas is fed from the bottom of the column. The gas and liquid are in contact due to the counter current flow. Finally, the CO_2 rich solvent flows out of the reactor from the bottom of the column and the flue gas is released from the exhaust to the atmosphere at the top of the column (Fitzgerald et al., 2014). As discussed above, the RPB is a special mode of PB. The amine solution enters the reactor from the inner boundary and leaves from the outer boundary of the bed and the

flue gas is fed from the outer boundary and leaves from the inner boundary of the bed. The solvent forms a thin film on the surface of the packing, which offers the maximum interfacial area in order to allow the CO_2 to be absorbed as much as possible.

The use of computational fluid dynamic (CFD) simulations is an effective tool to understand the flow behaviour and it can be applied for the future scale-up and optimized operation of these commercialized industrial reactors. In comparison with the experiments, numerical investigations of CO_2 absorption and desorption in post combustion could economize the manpower, material resource and time. The CFD simulation of post combustion CO_2 absorption in PBs/RPBs requires the combination of a flow dynamic, heat transfer, mass transfer and reaction models. In most literature on CO_2 absorption by liquid amine, they share much the same features, and have a similar mass transfer model and a reaction mechanism (Sebastia-Saez et al., 2014; Hosseini, et al., 2014). The novelty in these published literatures are that the new CFD models that accurately describe the multiphase flow in the new reactors.

Raynal et al. (2009) suggested that the CFD simulation of a multiphase reaction in the PBs could be performed via an original multi-scale approach from the liquid film thickness to the industrial column dimensions. For example, first model the micro-scale liquid wetting on the surface of the packing, then model the mesco-scale liquid film flow on the surface of the packing, and finally model the large-scale reactor by considering the PB as a porous bed. Generally, two methods, namely the Volume of Fluid (VOF) and Eulerian methods are used for modelling the flow dynamics in PBs. The differences in these two methods are as follows:

(i) The VOF focuses on modelling the liquid flow locally on the surface of the packing and it is suitable for micro-scale local simulations. However, it cannot simulate the whole reactor. The reason is that the VOF model requires a very small grid size to capture the droplets and film, so it is not suitable to simulate 3D or large pilot scale RPBs due to computer resource

limitations and the simulation time limitations. For example, a 3D model for a small RPB rig with the inner radius of 30 mm, the outer radius of 160 mm and the axial height of 50 mm requires about 1, 071,338 tetrahedral and 26, 190 pyramid grids (Yang et al., 2010) and Guo et al. (2017) also suggest about 1.6 million cells in total are required for a 3D wire mesh packing for VOF simulations. However, the Eulerian method can simulate the liquid flow through the whole bed with the appropriate mesh size and with the low requirement of computer resources.

(ii) The VOF method requires a transient simulation, which takes a much longer time, for example, approximately 60 hours running in parallel on a computer cluster, see [19], to achieve a simulation time step for 860,000 cells, which only forms part of the RPB reactor. However, for most cases, the flow in PBs/RPBs is a steady-state process and the Eulerian method can carry out the steady-state simulation and save much more computational time.

(iii) The VOF method can achieve a clear liquid surface to the air and does not need a special model to obtain the interfacial area whereas the Eulerian method gives a liquid fraction in a unit volume and cannot give the interfacial area through the simulation.

(iv) The VOF method treats the gas and liquid as one phase in the momentum equation and the only force considered for the interaction between the gas and liquid is the surface tension. In contrast, the Eulerian method treats the gas and liquid as individual phases. The method needs the porous media model to describe the flow resistance between the gas or liquid and the packing, the gas-liquid drag model and the interfacial area model to estimate the surface between the gas and liquid.

(v) For both methods, the challenge is the complexity of the gas and liquid flow through the PBs/RPBs. This is caused by the diversity in the packing patterns and structures. The packing materials could be random packing, such as random spheres or structured packing,

such as corrugated packing or wire screen packing. The accurate description of the gas or liquid flow through a great variety of packings using numerical simulations is very challenging.

When employing the VOF method on PBs, Raynal et al. (2007) and Sebastia-Saez et al. (2014, 2015) modelled the falling film flow and mass transfer locally on the surface of the packing on a micro-scale. Iso et al. (2013) compared two geometrical structured surfaces, namely smooth and wavy walls, using a CFD-VOF simulation and found that the surface texture treatments can assist in preventing the liquid channelling and increase the wetted area. All these investigations may give assistance to the simulation of the RPBs. Currently, the CFD simulation of the gas-liquid two-phase flow in RPBs only focus on the VOF method and the packing wire mesh was treated as being square or circular blocks in the 2D models and real structures in 3D models. Shi et al. (2013) developed a 2D multiphase VOF method to simulate the liquid flow in a RPB and the interface between the gas-liquid phases was clearly achieved. The formation of a film and droplets can clearly be observed from this method during transient simulations. Guo et al. (2016) combined the VOF multiphase model, the laminar finite-rate model and the Reynolds stress model to simulate the liquid concentration distribution and liquid flow velocity on the micromixing performance of a RPB, and the micromixing time was estimated to be 0.05 - 0.30 ms. Yang et al. (2016) used this method to investigate the liquid holdup and mass transfer of the dissolved oxygen released into the gas phase under different rotation speeds and liquid flow rates. Xie et al. (2017) investigated the effect of the rotation speed and contact angle on the MEA concentration liquid distribution and the formation of the liquid droplets by the VOF method. The difficulty in the VOF method for PBs/RPBs is the mesh generation and this is due to the complex packing structures. In order to perform the simulation conveniently and easily, and save computer memory resources, most researchers simplify the packing structures. For example, the

structure packing is simplified to be a tilted board, and the wire screen packing is simplified as square/circular blocks for 2D or vertical wires for 3D. However, these simplified structures are quite different from the real structures.

For the Eulerian method on PBs, Asendrych et al. (2013) and Niegodajew et al. (2016) used the porous media model to simulate CO_2 absorption by the liquid MEA solution in a 6mm-Raschig-rings randomly filled PB. Liu et al. (2006a) developed a turbulent mass transfer model for the CFD simulations of CO_2 removal using a NaOH aqueous solution in a pilot-scale ½inch-ceramic Berl-saddles randomly packed chemical absorption column. For the structured PB, Pham et al. (2015) and Kim et al. (2016) used the Iliuta porous media model and the Eulerian method to predict the gas and liquid two-phase flow and CO_2 capture from the flue gas. The number of published papers on the numerical investigation of CO_2 absorption in PBs is very limited and the publications on Eulerian simulations of the multiphase flow in the RPB are rare. The only paper that investigates the PRB is a conference paper, in which Martínez et al. (2012) used the Eulerian-Eulerian method to simulate the 3D gas-liquid flow in a RPB. Øi (2010) presented some challenges for the CFD simulations of the CO_2 capture by liquid amine and these are (i) unsolved gas/liquid interfacial area; and (ii) combination of different models, such as equilibrium and mass transfer, heat transfer and reaction models. On the other hand, the setting of the flow to be counter current is another difficulty. The boundary setup for the liquid inlet and outlet is challenging because the gas inlet and liquid outlet are overlapped and the gas outlet and liquid inlet are overlapped. In addition to these challenges, the toughest difficulty of the Eulerian method is how accurately the porous media model describes the gas and liquid flow and how the porous media model represents the differences in the packing materials. There are three popular porous media models in the literature: the Attou model (Attou et al., 1999), based on the spherical packing; the Lappalainen model (Lappalainen et al., 2008), based on the spherical packing and

wettability factor; and the Iliuta model (Iliuta et al., 2004), based on the structured packing and wettability factor. However, in the RPB, the wire screens are commonly used as the packing materials. The current available porous media models are not suitable for the wire screen packing. Up to now, it is still challenging to build a proper porous media model for some particular packing structures.

It can be seen that the Eulerian method should ideally be chosen for the CFD simulations of large pilot-scale RPBs. The purpose of this paper is to demonstrate the potential of employing the Eulerian porous media method for the efficient prediction of CO_2 absorption in a large-scale RPB. However, the difficulties for the Eulerian method in the simulation of RPBs are the settings for the counter-current flow, the porous media models and interfacial area. Therefore, the novelties of this work are as follows: (i) the application of a new gas-liquid two-phase porous media for wire screen packing based on the Kołodziej one-phase model (Kołodziej and Łojewska, 2009). The Kołodziej model treats the packing wire screens as small cylinders and not as traditional spheres and this takes into account the effect of the tortuosity on the fluid velocity through the packing; (ii) the interfacial area is derived from the VOF simulation of the liquid flow on the real wire screens; (iii) a more advanced reaction enhancement model is employed for describing liquid mass transfer; and (iv) the construction of the liquid generation and elimination zone to resolve the problem in the setting of the counter-current gas-liquid flow in the CFD simulation.

Finally, in this work, the CO_2 absorption in the RPB has been studied by the use of an Eulerian simulation based on the new settings for the gas-liquid counter-current flow, the new porous media model and the new interfacial area model.

2. Rotating packed bed for CO_2 absorption using MEA solutions

The simulation of CO_2 capture by MEA solutions in the RPB has been performed and this is based on the experiments in the RPB for CO_2 absorption by the liquid amine, which was

reported by Lee et al. (2017). A flowchart diagram of the whole process is shown in Fig. 1 and the dimension of the RPB is 80 mm for the inner diameter, 300 mm for the outer diameter and 20 mm for the width of the packed bed. The diameter of a polypropylene case for housing the RPB is 360 mm and the packing material is a stainless steel expanded mesh screen with a voidage of 0.801 and the surface area of 663 m^2/m^3.

The flue gas is stimulated by mixing air and CO_2 in the ratio 12 mol% CO_2 and preheated to 40 °C by a hot water system before entering the chamber cavity housed in a polypropylene case for the RPB on two sides through two pipes. After absorption, the gas leaves the RPB through the pipe that is connected to the inner boundary of the RPB.

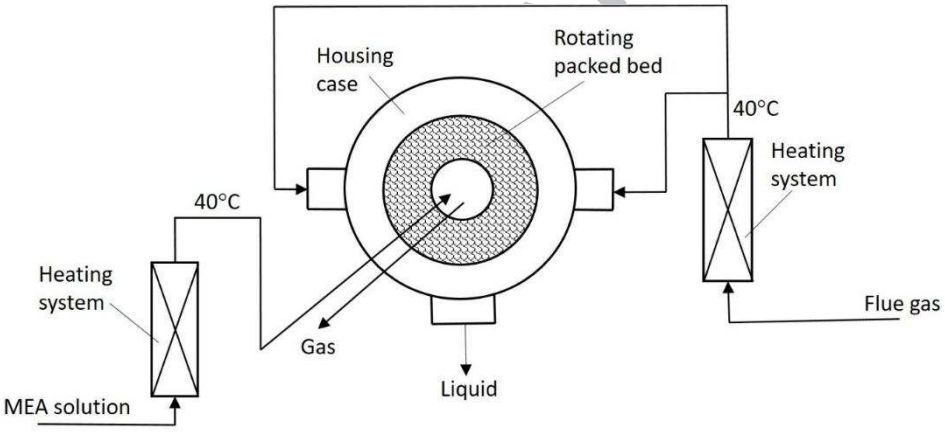

Fig. 1. Schematic diagram of the rotating packed bed for CO_2 absorption by the liquid amine.

The MEA solution with a mass fraction of 30% or 90% was first preloaded to 0.1 mol CO_2 / mol MEA. After that, the liquid was preheated to 40°C by a hot water system and then sprayed into the RPB from the centre using a 4 armed jet. After flowing through the packed wire screen, the liquid was thrown towards the case wall of the RPB and finally it is collected by a pipe that is situated at the bottom of the case.

The feed gas flow rate is 9.8 litres/s and the liquid to gas mass flow rate ratios are 2.8, 3.3 and 3.7 for the 30% MEA solutions, and 0.9, 1.0 and 1.2 for the 90% MEA solutions.

3. Simulation theory

The gas-liquid flow in the RPB investigated is a counter-current flow design. In the experimental rig, the RPB is closed in a polypropylene case as shown in Fig. 2(a). The gas passes the space between the case shell and the outer edge of the RPB enters into the RPB and finally flows out of the reactor through a central pipe. The liquid is sprayed onto the inner surface of the RPB and flows out of the RPB. After that, the liquid crosses the chamber cavity and finally collects on the wall of the polypropylene case.

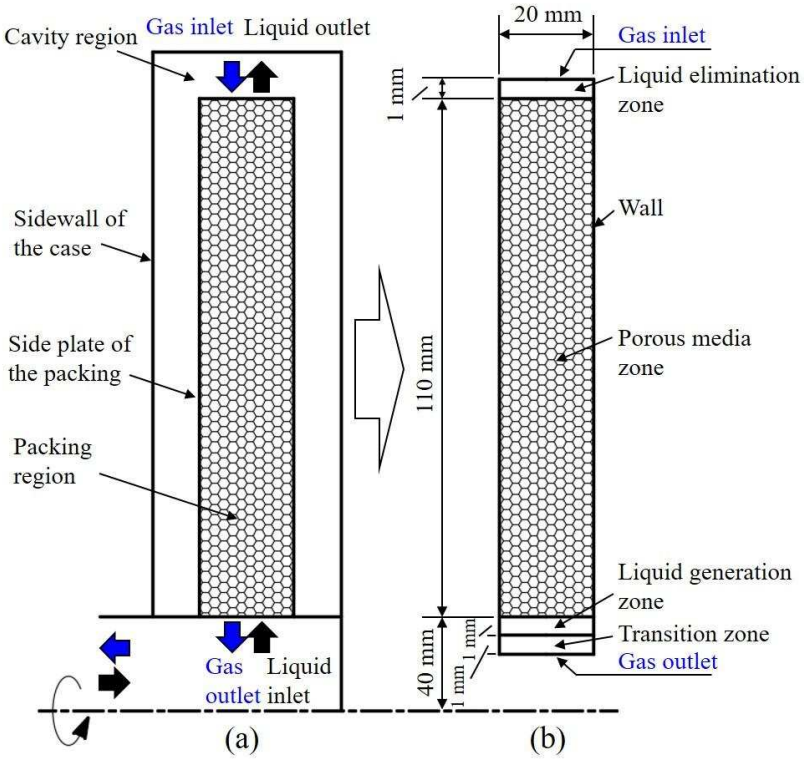

Fig. 2. Schematic diagram of the simulated physical model of the rotating packed bed (RPB). (a) model of the experimental RPB; (b) model of the simulation.

In order to easily perform the simulations, the complex gas swirl flow between the front side plate of the packing and the front sidewall of the polypropylene case and between the back side plate of the packing and the back sidewall of the polypropylene case are not included in this investigation since there is no experimental data available. The gas is assumed to enter uniformly through the outer boundary of the RPB. The chamber cavity that

is housed by a polypropylene case for the RPB is not considered and included as well. Thus, the geometry of the rig, as shown in Fig. 2(a), is simplified into the structure shown in Fig. 2(b). Because more reactions occur in the RPB, the dimension of the RPB has the same size as that in the real experimental rig and the gas outlet region is simplified into the area, which extends 10 mm from the inner boundary of the RPB. The simplified geometry represents the flow and reaction process in the RPB but omits the flow in the chamber cavity and the complex swirl flow between the front side plate of the RPB and the front sidewall of the case, and between the back side plate of the RPB and the back sidewall of the case.

The liquid flow in the RPB is almost axisymmetrical and this has been demonstrated in the experimental investigations (Yang et al., 2015). Thus, in this work, the 2D axisymmetric swirl Eulerian model is used to model the gas-liquid two-phase flow in the RPB. The rotation of the rig is simulated by the rotating reference frame. It should be noted that for a more detailed analysis, full 3D simulations should be performed.

The assumptions employed for the RPB are as follows: (i) the gas and liquid flows in the RPBs are in the steady state; (ii) the gas is incompressible; (iii) the liquid is usually sprayed into the packing by a number of uniformly distributed nozzles at the entrance to the RPB. The splashing of the liquid on the edge of the packing is complex but the liquid becomes uniformly dispersed very quickly with the assistance of the packing wires. Therefore, in this work, the liquid is treated as being a uniform flow that enters the packed bed for a given liquid flow rate; the details of the liquid entry region and the effect of the number of liquid spraying nozzles on the liquid flowing into the packing are not considered; (iv) once the liquid flows out of the packing, it will not have any impact on the flow in the packing. Therefore, in order to simplify the simulation, we assume that the liquid disappears immediately when the liquid flows out of the packing and reaches the liquid elimination zone;

and (v) in the packing region, the liquid flows in the form of films, droplets and rivulets. The interfacial area between the gas and liquid can be predicted using the VOF method.

The liquid flow and mass transfer process in packed beds are in the unsteady state, in particular at the micro-scale. For the RPB, when a limited number of liquid nozzles are used, it introduces unsteadies in the large scale. For the cases presented in this work, we take the view that the unsteadiness of the flow is a secondary phenomenon and the flow can be globally treated as being in a quasi-steady state, in particular this is valid when the number of the liquid nozzles employed are not too small. Nevertheless, the unsteady flow and mass transfer process caused by the limited number of liquid nozzles employed can be simulated by full 3D simulations using the same approach as presented in this paper. Further, the micro-scale unsteady flow and mass transfer process can be further simulated by the LES (Large Eddy Simulation) method with appropriate computer power.

The end effect of the liquid entry section was not included in this work. The liquid is usually sprayed into the packing by a number of uniformly distributed nozzles located at the entrance to the RPB. The splashing of the liquid on the edge of the packing is complex but the liquid becomes uniformly dispersed very quickly with the assistance of the packing wires. The liquid entry section is in a very limited region (Yang et al., 2015). Therefore, in this work, the liquid is treated as being a uniform flow that enters the packed bed; the details of the liquid entry region and the effect of the number of liquid spraying nozzles on the liquid flowing into the packed is not considered in detail. We take the view that this will not have a significant impact on the overall prediction of the CO_2 absorption efficiency of the packed bed especially when the size of the bed is large. This is the main aim of the development of this model. Furthermore, it is extremely challenging to simulate the very complex liquid splashing process at the entrance of the RPB in a counter-current flow configuration.

Additional models can be developed to be added on to the present porous media model and this is a future work.

A schematic diagram of the geometry and boundary conditions employed in the CFD simulations is shown in Fig. 2(b). The width of the bed is 20 mm. The distances of the gas outlet, liquid generation, inner boundary of the RPB, outer boundary of the RPB and the liquid elimination/gas inlet to the x-axis is 38 mm, 39 mm, 40 mm, 150 mm and 151 mm, respectively. The left and right sides of the whole bed are the wall boundary.

3.1 Governing equations

The governing equations are as follows:

(i) Mass equation:

$$\nabla \cdot \left(\rho_i \vec{v}_{ij}\right) = S_{m,i} \tag{1}$$

(ii) Momentum equation:

$$\nabla \cdot \left(\rho_i \vec{v}_{ij} \vec{v}_{ij}\right) = -\nabla P + \nabla \cdot \left(\bar{\bar{\tau}}_{ij}\right) + \vec{F}_{drag,j} - \vec{S}_{ij} \tag{2}$$

(iii) Species transport equation:

$$\nabla \cdot \left(\rho_i \vec{v}_{ij} Y_k\right) = -\nabla \cdot \vec{J}_{kj} + R_k \tag{3}$$

(iv) Energy equation:

$$\nabla \cdot \left(\vec{v}_i(\rho_i E_i + P)\right) = \nabla \cdot \left(k_{eff,i} \nabla T_i - \sum_k h_k \vec{J}_k + \left(\bar{\bar{\tau}}_{eff,ij} \cdot \vec{v}_{ij}\right)\right) + S_{h,i} \tag{4}$$

where, ρ is the density; v_{ij} is the fluid velocity (i = Gas or Liquid; j = the axial (x), radial (r) and tangential (z) coordinate direction); $S_{m,i}$ is the mass source; P is the pressure; τ_{ij} is the stress tensor; $F_{drag,j}$ is the drag force; S_{ij} is the momentum source; Y_k is the mass fraction of the species, such as CO_2 in the gas phase or MEA in the liquid phase (k = species); J_{kj} is the

mass diffusion flux; R_k is the production of the species by reaction; E_i is the total energy; $k_{eff,i}$ is the effective conductivity; h_k is the enthalpy of the species; $\tau_{eff,ij}$ is the effective shear tensor; and $S_{h,i}$ is the heat of chemical reaction.

3.2 liquid generation zone and elimination zone

One of challenges for the simulation of the gas-liquid counter-current flow is the boundary settings for the liquid inlet and liquid outlet. This is because there are no appropriate available boundary designs for the overlapped liquid inlet and gas outlet, and the overlapped liquid outlet and gas inlet. In order to overcome this difficulty, two zones for the liquid generation and elimination were constructed and the source equations for these two zones are described as follows:

(i) Liquid generation zone:

- For the liquid mass source,

$$S_{m,L} = \frac{Q_L \rho_L}{\pi({r_2}^2 - {r_1}^2)Z} \tag{5}$$

where, Q_L is the volume flow rate of the liquid; r_1 and r_2 are the radius of the liquid source zone; and Z is the thickness of the rotating packed bed.

(ii) Liquid elimination zone:

- For the liquid mass source,

$$S_{m,L} = -\left(\frac{\rho_L \alpha_L v_{x,L}}{\Delta x} + \frac{\rho_L \alpha_L v_{r,L}}{\Delta r} + \frac{\rho_L \alpha_L v_{r,L}}{r}\right) \tag{6}$$

- For the liquid momentum source,

$$S_{x,L} = -\left(\frac{1}{r}\frac{r \rho_L \alpha_L v_{x,L} v_{x,L}}{\Delta x} + \frac{1}{r}\frac{r \rho_L \alpha_L v_{r,L} v_{x,L}}{\Delta r}\right) \tag{7}$$

$$S_{r,L} = -\left(\frac{1}{r}\frac{r\rho_L\alpha_L v_{x,L}v_{r,L}}{\Delta x} + \frac{1}{r}\frac{r\rho_L\alpha_L v_{r,L}v_{r,L}}{\Delta r}\right) \quad (8)$$

$$S_{z,L} = -\left(\frac{1}{r}\frac{r\rho_L\alpha_L v_{r,L}v_{z,L}}{\Delta x} + \frac{1}{r}\frac{r\rho_L\alpha_L v_{x,L}v_{z,L}}{\Delta r}\right) \quad (9)$$

- For the species source,

$$S_j = -\left(\frac{\rho_L\alpha_L v_{x,L}Y_j}{\Delta x} + \frac{\rho_L\alpha_L v_{r,L}Y_j}{\Delta r} + \frac{\rho_L\alpha_L v_{r,L}Y_j}{r}\right) \quad (10)$$

- For the energy source,

$$S_{h,L} = -\left(\frac{\rho_L\alpha_L v_{x,L}H_L}{\Delta x} + \frac{\rho_L\alpha_L v_{r,L}H_L}{\Delta r} + \frac{\rho_L\alpha_L v_{r,L}H_L}{r}\right) \quad (11)$$

where, α_L is the liquid phase fraction; Δx is the axial size of the cell in the liquid elimination zone; Δr is the radial size of the cell in the liquid elimination zone; Y_j is the mass fraction of species; and H_L is the enthalpy of the liquid phase.

3.3 Porous media model

There are some porous media models for the gas-liquid two-phase flows in traditional packed beds, such as the Attou and the Iliuta models (Lu et al., 2018). The Attou model is derived from the spherical packings and the Iliuta model is derived from the structured-slit packings. However, the commonly used packings for the RPB are wire screens. The characteristics of the gas and liquid flows in these packings are different from those of traditional packings. Therefore, another challenge for the simulation using the Eulerian method is an appropriate porous media model for the RPBs. This is why there are very few publications for CFD simulation of multiphase reactions in RPBs. In this paper, a new porous media model for the RPBs, which has been previously constructed (Lu et al., 2018), is employed.

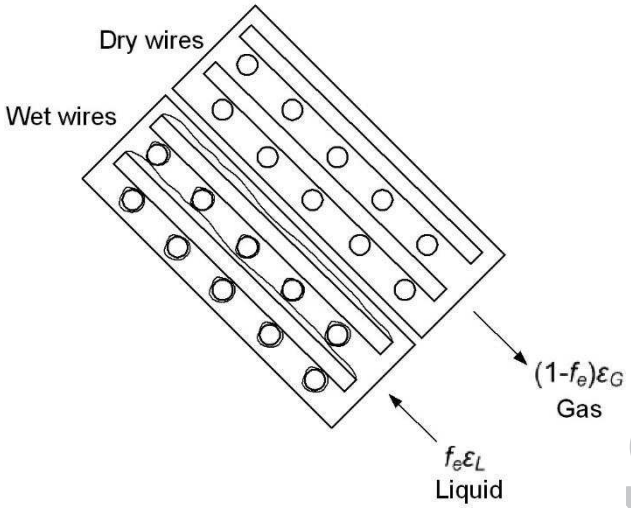

Fig. 3. Schematic diagram of the porous media model based on wet and dry wires.

The gas-liquid two-phase porous media model is derived from the Kołodziej one-phase model (Kołodziej and Łojewska, 2009). In order for this one-phase model to accommodate the gas-liquid two-phase flow, the concepts of wet wires and dry wires are introduced in this work. Thus, the surface of the packing is divided into a wet area, where the liquid flows through, and a dry area, where the gas crosses as shown in Fig. 3. Thus, the flow resistance for the liquid and gas can be derived from the one-phase flow resistance based on the Kołodziej equations, namely.

$$S_{LS} = f_e\varepsilon_L\left[4\left(f_{app}+f_t\right)\frac{\rho_L {v_L}^2}{2d_w}\frac{\varepsilon_S}{{\varepsilon_L}^3}\frac{\tau^3}{\cos^3\theta}\right] \tag{12}$$

$$S_{GS} = (1-f_e)\varepsilon_G\left[4\left(f_{app}+f_t\right)\frac{\rho_G {v_G}^2}{2d_w}\frac{(1-\varepsilon_G)}{{\varepsilon_G}^3}\frac{\tau^3}{\cos^3\theta}\right] \tag{13}$$

$$f_{app} = \frac{1}{Re_K}\left(\frac{3.44}{\sqrt{\chi^+}}+\frac{\frac{1.25}{4\chi^+}+16-\frac{3.44}{\sqrt{\chi^+}}}{1+\frac{0.00021}{{\chi^+}^2}}\right) \tag{14}$$

$$f_t = \frac{0.079}{{Re_K}^{0.25}} \tag{15}$$

$$\chi^+ = \frac{d_w}{D_h Re_K} \tag{16}$$

$$Re_K = \frac{\rho v_e D_h}{\mu} \tag{17}$$

For the gas-solids interaction:

$$\tau = 1 + \frac{\varepsilon_S}{2},\ d_w = \frac{4\varepsilon_S}{a_S},\ v_e = \frac{v}{\varepsilon_G}\frac{\tau}{\cos(\theta)},\ D_h = \frac{4\varepsilon_G}{a_S} \tag{18}$$

For the liquid-solids interaction:

$$\tau = 1 + \frac{\varepsilon_S}{2},\ d_w = \frac{4\varepsilon_S}{a_S},\ v_e = \frac{v}{\varepsilon_L}\frac{\tau}{\cos(\theta)},\ D_h = \frac{4\varepsilon_L}{a_S} \tag{19}$$

where, S_{LS} and S_{GS} are the resistances of the porous media for the liquid and gas phase; f_e is the fraction of the wetted area of the packing; ε_L and ε_G are the volume fraction of the liquid and gas phase; f_{app} is the fanning factor for laminar flows; f_t is the Fanning factor for turbulent flows; d_w is the wire size; τ is the tortuosity factor of the packing; D_h is the hydraulic diameter; Re_K is the Reynold number; v_e is the effective velocity; μ is the viscosity; a_S is the specific area of the dry packing; and $\theta = 60°$, which is estimated for the investigated packing structure and liquid flow (Lu et al., 2018).

The current porous media model is derived from only film flow. In fact, the film and droplets all exist in the porous media zone but the droplets are restricted by the wire mesh and interact with the film and the derived model is shown to be able to be extended for flows with a film and restricted droplets (Lu et al., 2018).

3.4 Gas-liquid drag model

In our previous work, we deduced F_{GL} as the drag force between the gas and liquid (Lu et al., 2018). The drag model is given by

$$F_{GL} = f_e \varepsilon_G \left[4\left(f_{app} + f_t\right)\frac{\rho_G (v_G - v_L)^2}{2d'_w}\frac{(1-\varepsilon_G)}{{\varepsilon_G}^3}\tau^3\right] \tag{20}$$

$$\tau = 1 + \frac{\varepsilon_S + \varepsilon_L}{2},\ d'_w = \frac{4\varepsilon_S}{a'_S},\ v_e = \frac{v\tau}{\varepsilon_G},\ D_h = \frac{4\varepsilon_G}{a'_S} \tag{21}$$

$$a'_S = \left(\frac{\varepsilon_L + \varepsilon_S}{\varepsilon_S}\right)^{\frac{1}{2}} a_S \tag{22}$$

where F_{GL} is drag force between the gas and liquid; a'_S is specific area of the wet wires; d'_w is wire and liquid film diameter.

3.5 Wire wettable fraction and interfacial area

In this work, the wire wettable fraction is assumed to be equal to the fraction of the interfacial area to the total area of the dry packing. Munjal et al. (1989b) and Luo et al. (2012) investigated the interfacial area between the gas and liquid in the RPBs. However, the derived correlations from these literatures are not suitable for general applications in the RPBs. The most general used correlation of the interfacial area in the RPB is the Onda equation (Tung and Mah, 1983; Liu et al., 1996; Tan and Chen, 2006; Joel et al., 2017). However, the Onda equation was originally obtained from measuring the absorption of CO_2 in the NaOH solution in the traditional packed beds. Therefore, there are still some controversial questions on how to properly define the variables in the Onda equation to fit the conditions of the RPB, e.g. the gravity, g in the traditional packed bed becomes the rotation acceleration, g_c in the RPB. In addition, the Onda equation has not been carefully examined by the experiments in the RPBs. Throughout our simulations, it is found that the results of the CO_2 absorption by liquid amine is very sensitive to the interfacial area and therefore the accurate equation for the prediction of the interfacial area is requested.

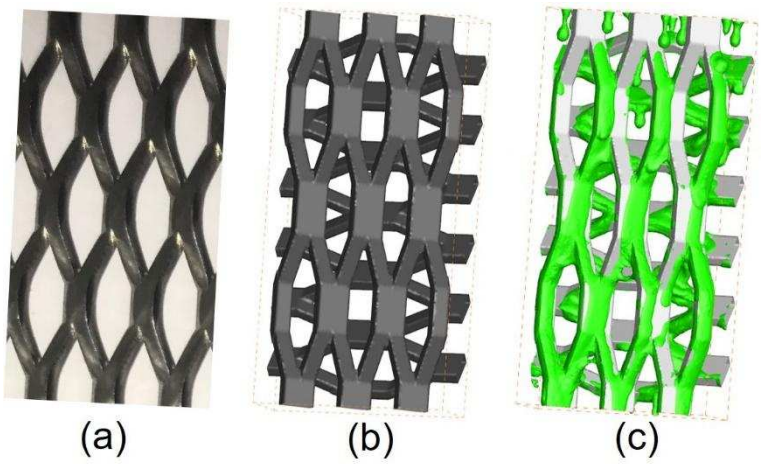

Fig. 4. VOF simulation of the liquid flow through the packing used in the real experiments. (a) packing mesh; (b) 3D model of the packing; and (c) modelled liquid flow through the packing.

In order to achieve the reasonable and correct interfacial area in this work, we simulated the local liquid flow on the packing meshes used in the experiments by the VOF method as shown in Fig. 4. From the simulation, the correlation for the effective interfacial area under the real experimental conditions in the RPB is obtained and given by Eq. (23) in Xie et al. (2018).

$$A_{GL} = 202.3485\left(\frac{g_c}{g_1}\right)^{0.0435}\left(\frac{U}{U_1}\right)^{0.4275}\left(\frac{\nu}{\nu_1}\right)^{0.1200}\left(\frac{\gamma}{\gamma_1}\right)^{-0.5856} \quad (23)$$

where, g_1 = 205.6 m/s^2, U_1 = 0.0106 m/s, ν_1 = 3.35×10^{-6} m^2/s and γ_1 = 75°; g_c is the rotation acceleration; U is the superficial liquid velocity; and γ is the dynamic contact angle. In this work, the dynamic contact angle, γ = 18°, means that the liquid easily spreads and contacts on the surface of the packing under the bed rotations (Sebastia-Saez et al., 2018; Xie et al., 2018).

The fraction of the interfacial area to the total area of the dry packing or the wet area to the total packing area is given by

$$f_e = \frac{A_{GL}}{a_S} \quad (24)$$

Considering the increment of the interfacial area from the wall next to the packing, the interfacial area in the wall region is estimated as follows:

$$A_{GL,w} = \left(A_w f_e + a_S f_e V_{cell,w}\right) = \left(\frac{1}{\Delta x_w} + a_S\right) f_e \quad (25)$$

where, the wet fraction of the wall is assumed to be the same as that in the packing region; A_w is the wall surface area in the cell next to the wall; $V_{cell,w}$ is the volume of the cell next to the wall; and Δx_w is the axial size of the cell next to the wall.

3.6 Mass transfer

For CO_2 absorption by the liquid amine, the mass transfer of CO_2 from the gas phase to the liquid phase was estimated using the following:

$$m_{GL,CO_2} = k_{GL} A_{GL} \left(\rho_{L,CO_2}{}^{*} - \rho_{L,CO_2}\right) \quad (26)$$

where, $m_{GL,CO2}$ is the transferred CO_2 mass between the gas phase and liquid phase; k_{GL} is the total mass transfer coefficient through the gas phase and liquid phase; $\rho_{L,CO2}$* is the CO_2 concentration on the surface of the liquid; and $\rho_{L,CO2}$ is the CO_2 concentration in the liquid bulk flow.

The two-film model was used to estimate the mass transfer coefficient between the gas and the liquid, namely

$$\frac{1}{k_{GL}} = \frac{RT}{H_{CO_2-MEA} k_G} + \frac{1}{k_L} \quad (27)$$

where, R is the gas constant; T is the temperature; $H_{CO2\text{-}MEA}$ is the Henry constant; k_G is the mass transfer coefficient in the gas phase; and k_L is the mass transfer coefficient in the liquid phase.

The liquid and gas mass transfer coefficients for the RPBs have been extensively investigated by many researchers. Munjal et al. (1989a) used the penetration theory and the complete convection diffusion model to predict the gas-liquid and liquid-solid mass transfer coefficients in the RPBs. Guo et al. (1997) used the NH_3 absorbed by water and SO_2 absorbed by the ammonium sulphite solution to investigate the mass transfer coefficients of the gas phase and liquid phase in the RPB. Chen et al. (2005a; 2005b; 2006) obtained correlations of the mass transfer coefficient for the liquid phase through the experiments in which the dissolved oxygen in the RPB was measured. Rajan et al. (2011) and Luo et al. (2012) used the absorption of CO_2 in the aqueous NaOH and investigated the interfacial area and liquid mass transfer coefficient. Zhao et al. (2014) summarized the mass transfer systems and different correlations for liquid mass transfer coefficients and gas mass transfer coefficients in the RPBs. There are numerous semi-empirical correlations based on different reaction and packing systems. However, these equations suffer from poor generalization performance (Zhao et al., 2014). Therefore, the mass transfer coefficients for the gas and liquid phase from these literatures are not applied in this work.

In this work, the Hughmark model (Fluent, 2013) was employed for the mass transfer coefficient in the gas phase because this model can predict the mass transfer coefficient for a wider range of relative Reynolds numbers. The mass transfer coefficient between the gas and liquid is dominated by the mass transfer in the liquid. Therefore, the mass transfer model for the gas phase does not significantly influence the results.

For the mass transfer coefficient in the liquid phase, the second-order irreversible enhancement model is used because the CO_2 absorption can be simplified as a second-order irreversible reaction. The reasons are (i) the CO_2 absorption reaction is a Zwitterionic mechanism. The CO_2 reaction rate is $r_{CO_2} = -\frac{k_2[MEA][CO_2]}{1+\frac{k_{-1}}{k_b[MEA]}}$, but $\frac{k_{-1}}{k_b[MEA]} \ll 1$. Therefore, the

CO_2 reaction rate can be estimated by $r_{CO_2} = -k_2[MEA][CO_2]$. Therefore, this reaction can be simplified as the second-order irreversible reaction for describing the CO_2 absorption process; (ii) this simplification can make the simulation much easier without losing the prediction accuracy at the temperature range for CO_2 absorption; (iii) this simplified method has been extensively employed in the simulations of the CO_2 absorption (Hosseini et al., 2014; Sebastia-Saez et al., 2014; Niegodajew and Asendrych, 2016).

The second-order irreversible enhancement model is given by

$$k_L = E_x k_L^* \tag{28}$$

where, E_x is the enhancement factor.

Here, we assume the film theory as mass transfer process in the liquid. The mass transfer coefficient in film theory, k_L^*, is given by:

$$k_L^* = \frac{D_{L,CO_2}}{\ell} \tag{29}$$

where, $D_{L,CO2}$ is the diffusivity of CO_2 in the liquid phase; and ℓ is the diffusion layer thickness for mass transfer.

In the literature (Levich, 1962), the diffusion layer thickness for the rotating disk has been found to be a function of the diffusivity, kinematic viscosity of the liquid and the angular velocity of the RPB, i.e. Mooney et al. (1981) estimated the values of the diffusion layer thickness as being 1.67 - 2.29×10^{-3} cm for the dissolution of the solid Benzoic acid, 2-Naphthoic acid and Indomethacin in the KCL solutions for rotational speeds up to 900 rpm. Jeannot and Cantwell (1997) measured the extraction of the 4-MAP from water into n-Octane with different stirring rates and obtained 1.69×10^{-3} cm for the stirring rate of 900 rpm and 1.24×10^{-3} cm for the stirring rate of 1200 rpm. Wegner (2017) presented an example of CO_2 being scrubbed by water flowing through a packed bed and the diffusion layer thickness is

7.6×10^{-3} cm. Thus it can be seen that the diffusion layer thickness changes with different liquid viscosities and rotating speeds but the range in the diffusion layer thicknesses is limited from 1.0×10^{-3} cm to 8.0×10^{-3} cm.

In order to examine the effect of the diffusion layer thickness on the CO_2 absorption, we compared the CO_2 mass fraction at the gas outlet under different diffusion layer thicknesses (1.0×10^{-3} cm, 5.0×10^{-3} cm and 8.0×10^{-3} cm) for the 30% MEA solution and 90% MEA solution at the rotation speed of 850 rpm. For the 30% MEA solution, the mass fraction of CO_2 at the gas outlet is 0.135928, 0.135951 or 0.135974 and for the 90% MEA solution, the mass fraction of CO_2 at the gas outlet is 0.135199, 0.135201 or 0.135204, respectively, for the diffusion layer thickness of 1.0×10^{-3} cm, 5.0×10^{-3} cm or 8.0×10^{-3} cm. This shows that the CO_2 absorption is not sensitive to the diffusion layer thickness. Therefore, the diffusion layer thickness of 5.0×10^{-3} cm is employed for all the cases investigated. Nevertheless, in the modelling, the diffusion layer thickness can be set as a variable if required by the simulation.

The enhancement factor is given by (Wellek et al., 1978):

$$E_x = 1 + ((E_i - 1)^{-1.35} + (E_1 - 1)^{-1.35})^{-\frac{1}{1.35}} \tag{30}$$

$$E_i = 1 + \frac{D_{L,MEA} C_{L,MEA}}{2 D_{L,CO2} C_{L,CO2}} \tag{31}$$

$$E_1 = \frac{Ha}{tanh(Ha)} \tag{32}$$

$$Ha = \sqrt{\frac{k_2 D_{L,CO2} C_{L,MEA}}{(k_L^*)^2}} \tag{33}$$

where, $C_{L,MEA}$ and $C_{L,CO2}$ are the mole concentrations of MEA and CO_2 in the liquid phase; Ha is the Hatta number; and k_2 is the reaction rate constant.

The CO_2 saturation concentration on the liquid surface is given by:

$$\rho_{L,CO_2}{}^{*} = M_{w,CO_2} \frac{P_{CO_2}}{H_{CO_2-MEA}} \quad (34)$$

where, $M_{w,CO2}$ is the molar mass of CO_2; $H_{CO2\text{-}MEA}$ is the Henry constant of CO_2 in the MEA-water solution; and P_{CO2} is the partial pressure of CO_2 in the gas phase.

The Henry constant was estimated by the N_2O analogy method (Penttilä et al., 2011) as follows:

$$H_{CO_2-MEA} = H_{N_2O-MEA} \left(\frac{H_{CO_2}}{H_{N_2O}}\right)_w \quad (35)$$

where, $H_{N2O\text{-}MEA}$ is the Henry constant of N_2O in the MEA-water solution; H_{CO2} is the Henry constant of CO_2 in water; and H_{N2O} is the Henry constant of N_2O in water.

The diffusivity of CO_2 in the MEA solution was estimated by the N_2O analogy method (Liu et al., 2006b) as follows:

$$D_{L,CO_2} = D_{L,N_2O} \left(\frac{D_{CO_2}}{D_{N_2O}}\right)_w \quad (36)$$

The diffusivity of the MEA molecules in the MEA solution is given by Snijder et al. (1993) as follows:

$$D_{L,MEA} = exp\left(-13.275 - \frac{2198.3}{T} - 0.078142 C_{L,MEA}\right) \quad (37)$$

3.7 Heat transfer

The transferred heat between the gas and the liquid is given by

$$Q_{h,GL} = h_{GL} A_{GL} (T_G - T_L) \quad (38)$$

where, $Q_{h,GL}$ is the transferred heat between the gas and liquid; h_{GL} is the heat transfer coefficient; A_{GL} is the interfacial area between the gas and liquid; and T_G and T_L are the temperatures of the gas and liquid, respectively.

There are very few publications reporting the heat transfer in the RPBs. In this work, the Hughmark model (Hughmark, 1967) was used for predicting the heat transfer coefficient between the gas and the liquid, h_{GL}, as follows:

$$h_{GL} = \frac{\kappa_L Nu_G}{d_p} \tag{39}$$

$$Nu_G = 2.0 + 0.6 Re_G^{\frac{1}{2}} Pr_L^{\frac{1}{3}} \quad 0 \le Re_G < 776.06, 0 \le Pr_L < 250 \tag{40}$$

$$Nu_G = 2.0 + 0.27 Re_G^{0.62} Pr_L^{\frac{1}{3}} \quad 776.06 \le Re_G, 0 \le Pr_L < 250 \tag{41}$$

where, d_p is the equivalent diameter of the liquid droplet; κ_L is the thermal conductivity of the liquid phase; Nu_G is the Nusselt number of the gas phase; and Pr_L is the Prandtl number of the liquid phase.

The wall of the RPB is treated as being adiabatic.

3.8 Reaction model

The absorption of CO_2 by MEA can be described by the Zwitterionic mechanism with two-step reactions (Ma et al. 2015; Wang et al., 2013). The first step is to form a Zwitterion as an intermediate and the second step is for the Zwitterion to react with a base, such as a MEA, to deprotonate. The two-step reactions are given as follows:

$$CO_2\,(L) + HOC_2H_4NH_2\,(L) \underset{k_{-1}}{\overset{k_2}{\rightleftharpoons}} HOC_2H_4NH_2{}^{+}COO^{-}\,(L)$$

$$HOC_2H_4NH_2{}^{+}COO^{-}\,(L) + HOC_2H_4NH_2\,(L) \xrightarrow{k_b} HOC_2H_4NH_3{}^{+}\,(L) + HOC_2H_4NHCOO^{-}\,(L)$$

The CO_2 reaction rate is given by:

$$r_{CO_2} = -\frac{k_2[MEA][CO_2]}{1+\frac{k_{-1}}{k_b[MEA]}} \tag{42}$$

where, r is the reaction rate; k_2, k_{-1} and k_b are the reaction rate constant; [MEA] and [CO_2] are the molar concentration.

The total reaction is given by:

$$CO_2\,(L) + 2HOC_2H_4NH_2\,(L) \overset{k_2}{=} HOC_2H_4NH_3^+\,(L) + HOC_2H_4NHCOO^-\,(L) \quad (43)$$

The CO_2 reaction with the MEA can be treated as a second-order irreversible reaction because $\frac{k_{-1}}{k_b[MEA]} \ll 1$ and the CO_2 reaction rate can be simplified as follows:

$$r_{CO_2} = -k_2[MEA][CO_2] \quad (44)$$

This simplified reaction has been extensively used in the simulation of CO_2 absorption by the liquid amine (Hosseini et al., 2014; Sebastia-Saez et al., 2014; Niegodajew and Asendrych, 2016). In this work, the formation enthalpies of $HOC_2H_4NH_3^+$ and $HOC_2H_4NHCOO^-$ are derived from the literature (Mishra, 2014).

In this work, we used the equation for the reaction rate constant,

$$k_2 = 4.4 \times 10^{11} exp\left(-\frac{5400}{T}\right) \quad (45)$$

which was proposed by Verstege et al. (1996) and it has been used by Hosseini et al. (2014).

Aboudheir et al. (2013) reviewed the reaction rate constant for the CO_2 absorption by the MEA from different experiments, e.g. Hikita et al. (1977), Verstege et al. (1996) and Horng and Li (2002). Many simulations on CO_2 absorption by MEA solutions have used the Hikita reaction rate constant (Pham et al., 2015; Sebastia-Saez et al., 2015; Niegodajew and Asendrych, 2016). Actually, these obtained reaction rate constants for the CO_2 absorption by the MEA are very similar.

4 Simulation conditions and method

During the simulations, the gas phase consists of CO_2 and air and the liquid phase is composed of CO_2, MEA ($HOC_2H_4NH_2$), $MEAH^+$ ($HOC_2H_4NH_3^+$), $MEACOO^-$ ($HOC_2H_4NHCOO^-$) and water. The properties of the materials and the operating conditions are shown in Table 1. According to the literature (Amundsen et al., 2009), the density of the MEA solutions change very slightly with the variations in the temperature but the viscosity is very sensitive to the temperature. Therefore, in the simulation, the liquid density is assumed to be constant and the correlation of the viscosity with the temperature was achieved from the data presented in the literature (Amundsen et al., 2009).

The properties of the phases, such as the thermal conductivity, specific heat for the liquid or gas phases are all estimated by the mixing law based on the different species in each phase. In the experiment, both the 30% and 90% MEA solutions were preloaded to 0.1 mol CO_2/mol MEA before the absorption of CO_2 in the flue gas. In the simulations, we assumed that the preloaded CO_2 in the liquid phase all reacted with the MEA and finally formed $MEAH^+$ and $MEACOO^-$ in the solution. 18 cases based on different L/G mass ratios, e.g. L/G = 2.8, 3.3, 3.7 for 30% MEA, L/G = 0.9, 1.0, 1.2 for 90% MEA and different rotation speeds, e.g. 600, 850, 1150 rpm were simulated in this work. The swirl velocity at the gas inlet is assumed to have the same rotation speed as in the packing region and does not consider the gas acceleration along the tangential direction because the gas inlet is very close to the outer boundary of the packing. Thus, the gas inlet boundary is set as the inlet velocity v_r = 0.5167 m/s and the inlet temperature of 313.2 K and the gas outlet boundary is set as the pressure-outlet. The liquid is generated from the liquid generation zone and the temperature is fixed at 313.2 K. Finally, the liquid disappears in the liquid elimination zone. The wall boundary is set as the no slip and adiabatic wall. The mesh cell size is 0.25 mm (length) × 0.01 mm (width).

Table 1
Properties of the phases and the operating conditions for the simulations.

Properties of phases	Settings	Conditions	Settings
Density of gas phase	Incompressible ideal gas	Gas flow rate	9.8 l/s
Density of liquid phase	1003.4 kg/m^3 for 30% MEA* 1000.6 kg/m^3 for 90% MEA*	Liquid/Gas mass flow rate ratio (L/G) for 30% MEA	2.8, 3.3, 3.7
Viscosity of gas phase	Mixing law	Liquid/Gas mass flow rate ratio (L/G) for 90% MEA	0.9, 1.0, 1.2
Viscosity of liquid phase	$\mu_{0.3}$ for 30% MEA*† $\mu_{0.9}$ for 90% MEA*‡	Initial temperature for gas inlet	313.2 K
Specific heat of gas phase	Mass weighted mixing law	Initial temperature for liquid inlet	313.2 K
Specific heat of liquid phase	Mass weighted mixing law	Gas outlet	Pressure outlet, P_{out} = 0 Pa
Thermal conductivity of gas phase	Mass weighted mixing law	Wall boundary	No slip wall Adiabatic wall
Thermal conductivity of liquid phase	Mass weighted mixing law	Mass fraction in the gas phase	CO_2: 0.1697 Air: 0.8303
Mass diffusivity of gas phase	Kinetic theory	Mass fraction in the liquid phase for 30% MEA solution (after preloaded CO_2: 0.1 mol CO_2/1 mol MEA)	CO_2: 0.0 $MEACOO^-$: 0.0501 $MEAH^+$: 0.0298 MEA: 0.2349 H_2O: 0.6852
Mass diffusivity of liquid phase	Kinetic theory	Mass fraction in the liquid phase for 90% MEA solution (after preloaded CO_2: 0.1 mol CO_2/1 mol MEA)	CO_2: 0.0 $MEACOO^-$: 0.1441 $MEAH^+$: 0.0859 MEA: 0.6761 H_2O: 0.0939

* From the literature (Amundsen et al., 2009)
† $\mu_{0.3} = 0.3083 - 0.00262T + 7.4882 \times 10^{-6}T^2 - 7.17293 \times 10^{-9}T^3$ (Pas)
‡$\mu_{0.9} = 4.37711 - 0.03776T + 1.08945 \times 10^{-4}T^2 - 1.05031 \times 10^{-7}T^3$ (Pas)
$298\text{K} \leq \text{T} \leq 353\text{K}$

The uncertainties associated with the experimental results may bring the discrepancy between the simulation and experiments. These uncertainties are (i) the CO_2 concentration is measured at the gas inlet and outlet pipes and it is not measured directly from inside the packed bed. The influence of the residence time on the separation between the gas and liquid on the absorption is not known; (ii) the complex gas-liquid vortex flow in the space between the front sidewall of the case and front side plate of the packing, and the space between the

back sidewall of the case and back side plate of the packing introduces some uncertainties in the CO_2 absorption results; (iii) the gas and liquid flows in the cavity are very complex. The liquid flows as a wide range of droplets with different sizes. The gas forms the free vortex and this causes the reaction uncertainties; (iv) in the liquid entry region, the liquid is sprayed onto the packing almost uniformly but this may not completely uniformly enter into the bed because of the limitation of the nozzle number.

The simulation details can be found in the publication (Lu et al., 2018). The 2D axisymmetric laminar flow model is used for the CFD simulation of the RPB. For the Kołodziej flow resistance equation, the "laminar flow" means the viscous flow corresponding to the viscous part of the flow resistance equation; the "turbulent flow" means the inertial flow corresponding to the inertial part of the flow resistance equation. From the view of fluid mechanics, the flow regimes for porous media are: (i) $Re \leq 1$, creeping or Darcian regime; (ii) $1 < Re < 500$, nonlinear-laminar or viscous-inertial regime; (iii) $Re \geq 500$, turbulent regime (Hlushkou and Tallarek, 2006). For the cases investigated in this work, Re_L is about 2.2, thus indicating the nonlinear laminar flow or the viscous-inertial regime. Thus in the CFD simulations, we have used the laminar model to simulate the flow and the flow resistance equation employed includes both the viscous and inertial contributions. The porous formulation is based on the superficial velocity. For the solver, the pressure based method and the relative velocity formulation were employed. During the simulations, the COUPLE method was employed. The second-order upwind discretisation schemes were used for the momentum, swirl velocity and all the species equations and the QUICK discretisation scheme was used for the volume fraction equation. The convergent conditions are that the residuals for all the equations are less than 1×10^{-3} and all the residuals reach stable and do not change. A mesh independence has been checked based on the meshes of 50×113, 100×226, 150×339

and 200×452, and the pressure deviation is within 0.2%. The simulation software employed is Fluent 16.1.0.

5 Results

5.1 Liquid holdup

The characteristics of the liquid holdup distribution is one of main physical behaviours for the gas-liquid two-phase flow in the RPB. The liquid holdup is defined as follows:

$$h_L = \frac{V_L}{V_{reactor}} = \varepsilon \alpha_L \tag{46}$$

where V_L is the volume of the liquid in the bed; $V_{reactor}$ is the volume of the reactor; ε is the porosity of the packed bed; α_L is the liquid phase fraction.

The contours of the liquid holdup in the bed and the liquid holdup distribution curves along the radial direction on the centreline of the bed are shown in Fig. 5. Figs. 5(a) and 5(b) are the contour figures for the 30% MEA and 90% MEA solutions, respectively, and all these show distributions along the axial and radial directions. Fig. 5(c) shows the detailed liquid holdup distributions of the 30% and 90% MEA solutions along the bed centreline in the radial direction.

It can be seen from Fig. 5 that in the packing region, the liquid holdup decreases with the radial distance from 0.022 (30% MEA) or 0.014 (90% MEA) at the inner boundary of the liquid source to 0.003 (30% MEA) or 0.002 (90% MEA) at the outer boundary of the packing. Fig. 5(c) shows that the liquid holdup for the 30% MEA is higher than that for the 90% MEA. The reason is that during the simulations and experiments, the gas volume rate is fixed at 9.8 litres/s and thus, the liquid inlet velocity for the 30% MEA solution with L/G = 3.3 is higher than that of the 90% MEA solution with L/G = 1.0.

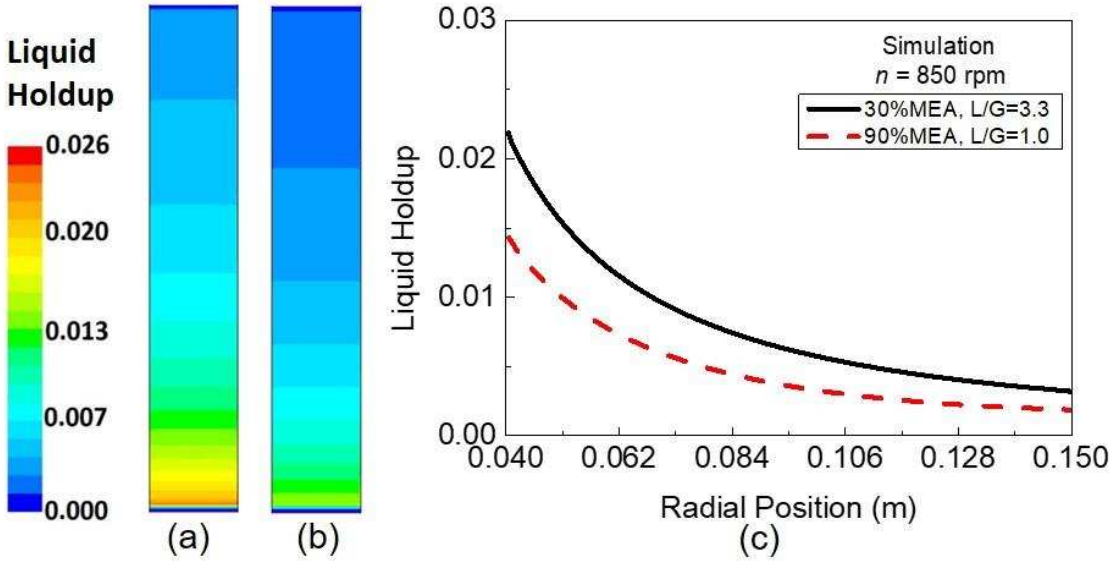

Fig. 5. Contours of the liquid holdup (a) 30% MEA, L/G = 3.3, n = 850 rpm; (b) 90% MEA, L/G = 1.0, n = 850 rpm, and the liquid holdup as a function of radial position for the different MEA solutions; and (c) along the bed centreline in the radial direction.

Next, we focus on the liquid holdup distribution in the RPB. In order to compare the simulation results with the experimental data, the Burns correlation (Burns et al., 2000) is used. Generally, the rotating packed bed uses a very high porosity of wire packing (generally more than 80%). Therefore, the Burns correlation treats the influence of the porosity on the liquid holdup very briefly and the influence of the porosity is not considered in the correlation. However, the Burns correlation is widely accepted by many researchers and it is used in the process simulations (Kang et al., 2014; Joel et al., 2017). The Burns experimental correlation (Burns et al., 2000) for the liquid holdup is given by

$$h_L = 0.039 \left(\frac{g_c}{g_0}\right)^{-0.5} \left(\frac{U}{U_0}\right)^{0.6} \left(\frac{\nu}{\nu_0}\right)^{0.22} \quad (47)$$

where g_0 = 100 m/s^2; U_0 = 1 cm/s; v_0 = 1 cS; h_L is the liquid holdup; g_c is the rotation acceleration; U is the superficial velocity; and ν is the kinematic viscosity.

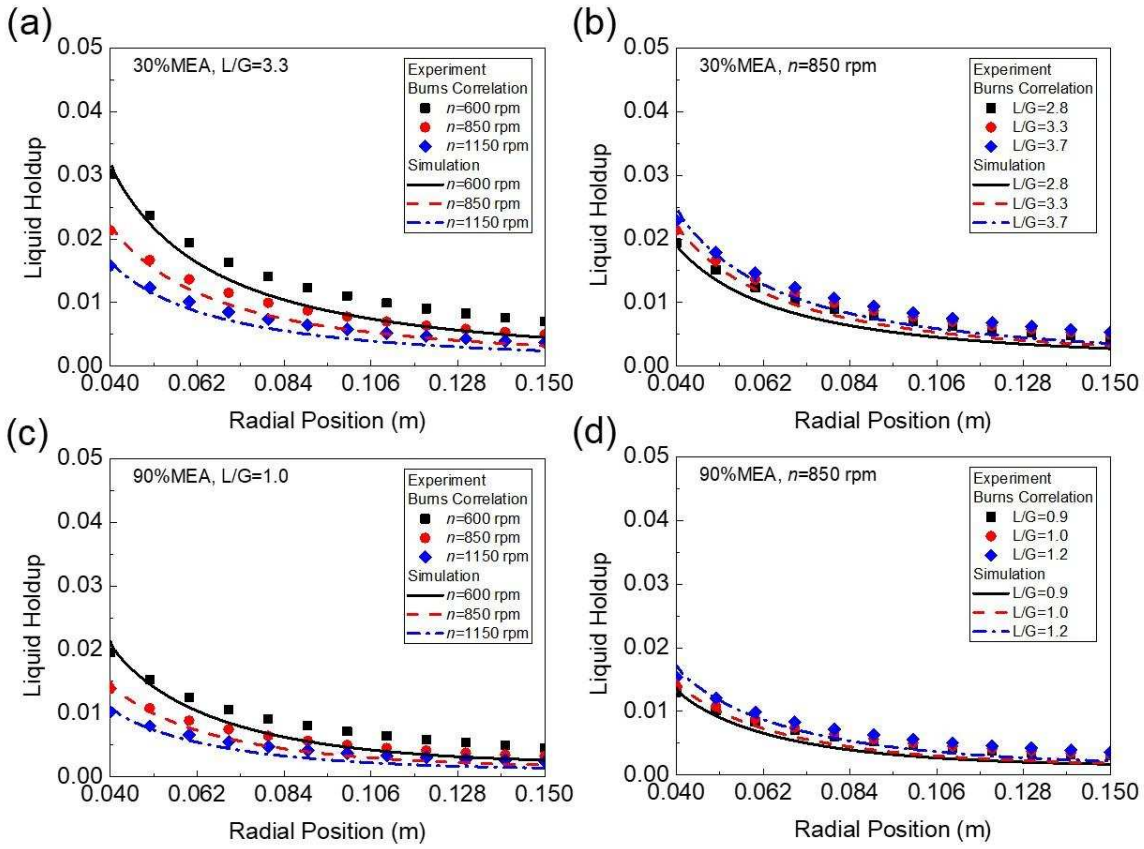

Fig. 6. Comparison of the liquid holdup between the simulation and the Burns correlation (Burns et al., 2000).

A comparison of the liquid holdup between the simulation results and the Burns correlation is shown in Fig. 6. Figs. 6(a) and 6(c) show that the liquid holdup for the 30% and 90% MEA solutions under different rotation speeds of 600, 850 and 1150 rpm. Figs. 6(b) and 6(d) show the liquid holdup for the 30% and 90% MEA solutions under different L/G ratios.

Fig. 6 indicates that for both the simulations and the experiments, with increasing the rotation speed, the liquid holdup decreases; with increasing the L/G ratio, the liquid holdup increases. This is because the gas flow rate is fixed at 9.8 litres/s and the higher L/G ratio gives rise to a higher liquid inlet velocity. It is found that when the liquid enters the packing area, the liquid holdup predicted by the CFD is close to the Burns correlation. For example, at the inner boundary of the RPB (r = 0.04 m), the liquid holdup with 30% MEA (L/G = 3.3, n = 850 rpm) are 0.0219 and 0.0213 for the simulation and the Burns correlation values,

respectively, and thus the relative standard deviation for the simulation is about 2.8%. At the same radial position, the liquid holdup of 90% MEA (L/G = 1.0, n = 850 rpm) are 0.0149 and 0.0138 for the simulation and the Burns correlation values, respectively, and the relative standard deviation is about 8.0%. In the regions near the packing outer boundary, the predicted values are lower than the Burns correlation values. For example, at the outer boundary of the RPB (r = 0.015 m), the liquid holdup with 30% MEA (L/G = 3.3, n = 850 rpm) are 0.0032 and 0.0050 for the simulation and the Burns correlation values, respectively, and the relative standard deviation is 36.0%. At the same position, the liquid holdup with 90% MEA (L/G = 1.0, n = 850 rpm) are 0.0018 and 0.0032 for the simulation and Burns correlation values, respectively, and the relative standard deviation is about 43.8%. If the error is given by (Lu et al., 2016),

$$\delta_{sim} = \frac{\sqrt{\sum_{i=1}^{i=N} |h_{Li,sim} - h_{Li,exp}|^2}}{\sqrt{\sum_{i=1}^{i=N} h_{Li,exp}{}^2}} \tag{48}$$

then the errors are 16.4%, 15.8% and 15.3% for the 30% MEA solution (L/G = 3.3) under the rotation speeds of 600 rpm, 850 rpm and 1150 rpm, respectively, and the errors are 19.0%, 15.8% and 14.2% for the 30% MEA solution (n = 850 rpm) under the rotation speeds of L/G = 2.8, 3.3 and 3.7 respectively. The errors are 20.8%, 20.5% and 20.3% for the 90% MEA solution (L/G = 1.0) under the rotation speeds of 600 rpm, 850 rpm and 1150 rpm respectively, and the errors are 22.5%, 20.5% and 17.7% for the 90% MEA solution (n = 850 rpm) under the rotation speeds of L/G = 0.9, 1.0 and 1.2, respectively. In summary, most errors are within 25%.

For all the cases investigated, the simulated flow behaviours agree with the experimental observations and the predicted liquid holdup matches the Burns correlation. In conclusion, it has been demonstrated that the CFD simulations presented in this work is reasonable and effective for predicting the flows in the RPBs.

5.2 CO_2 absorption

The interfacial area and the mass transfer coefficient are two key factors influencing CO_2 absorption. Fig. 7(a) shows the variation of the interfacial area calculated by Eq. (23) with the radial position for the 30% MEA and 90% MEA solutions. It indicates that the interfacial area of the 30% MEA solution is larger than that of the 90% MEA solution, and this is due to the higher liquid flow rate for the 30% MEA solution. Fig. 7(b) shows the variation of the mass transfer coefficient calculated by Eq. (27) with the radial position for the 30% MEA and 90% MEA solutions. In the bed region of r = 0.040 - 0.065 m, the mass transfer coefficient of 90% MEA is lower than that of the 30% MEA. This is because the high concentration MEA has higher viscosity and lower diffusivity than the low concentration MEA solution, which causes the lower mass transfer coefficient. However, the gradient of the mass transfer coefficient for the 90% MEA solution is much higher than that for the 30% MEA solution, and this is due to the much higher predicted enhancement factor in Eq. (30), which is the ratio of the chemical absorption flux to the physical absorption flux. The enhancement factor has a positive relationship with the MEA solution and k_2 due to the higher temperature, which is caused by the release of reaction heat. Therefore, the higher amount of CO_2 absorbed by the 90% MEA solution in the RPB is attributed to the higher enhancement factor. In the bed region of r = 0.130 - 0.150 m, the mass transfer coefficient of the 90% MEA solution slightly decreases due to the decrease of the liquid temperature caused by the heat exchange between the liquid phase and gas phase.

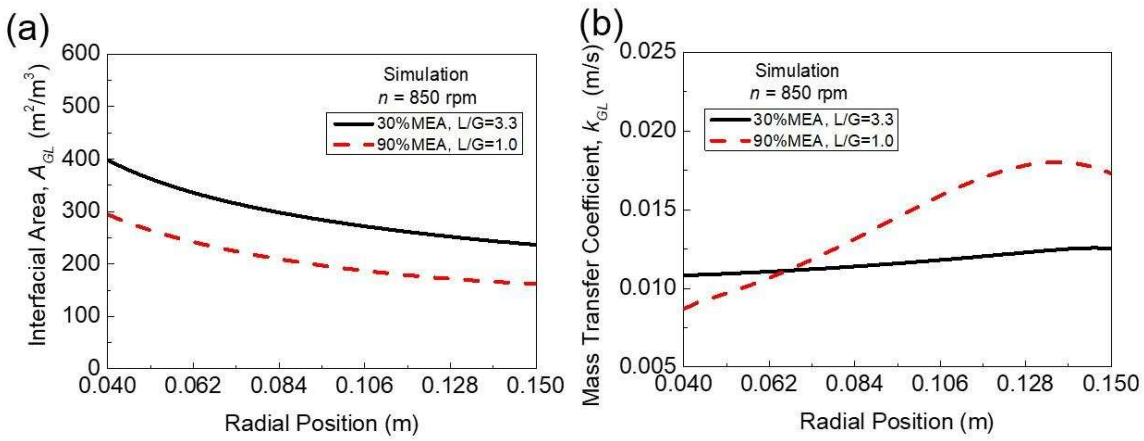

Fig. 7. Mass transfer as a function of the radial position for the different MEA solutions along the bed centreline in the radial direction. (a) interfacial area, A_{GL}; and (b) mass transfer coefficient, k_{GL}.

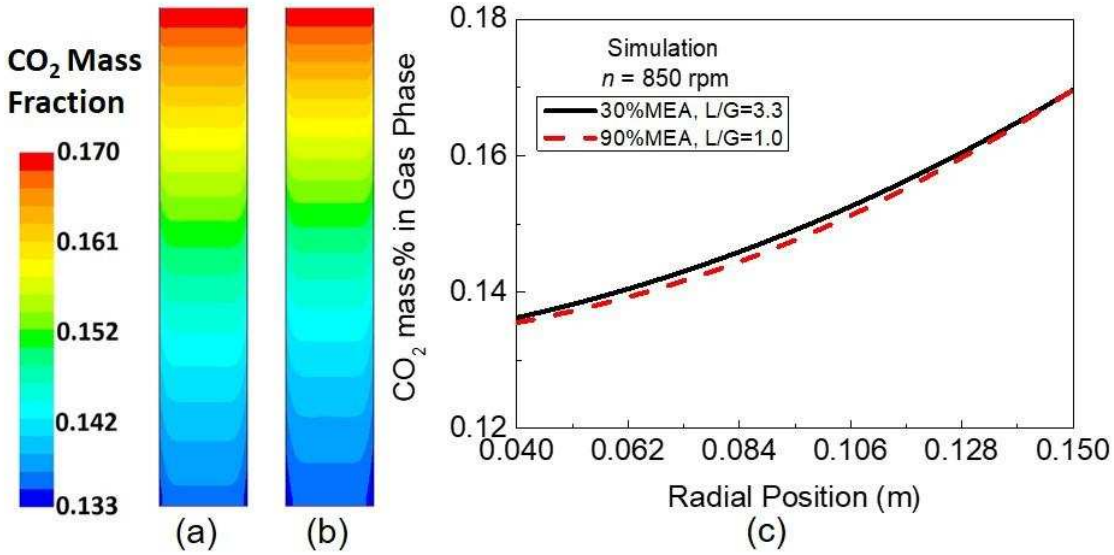

Fig. 8. Contours of the CO_2 mass fraction in the gas phase (a) 30 % MEA, L/G = 3.3, n = 850 rpm; (b) 90 % MEA, L/G = 1.0, n = 850 rpm; and (c) CO_2 mass fraction as a function of the radial position for the different MEA solutions along the bed centerline in the radial direction.

The absorption of CO_2 by the liquid amine is characterised by the change of the CO_2 concentration in the gas phase in the reactor. Fig. 8 shows the CFD predicted contours of the CO_2 mass fraction with (a) 30 % MEA, and (b) 90 % MEA, and the distribution of the CO_2

mass fraction (c) along the bed centerline. This shows that the CO_2 mass fraction decreases from 0.1697 at the gas inlet to 0.1363 (30% MEA) or 0.1355 (90% MEA) at the inner boundary of the packing. The contour figures show that at the same radial position, the CO_2 mass fraction is the highest in the central region of the bed and then it decreases towards the sidewall of the RPB. This is because the sidewalls increase the interfacial area as shown in Eq. 25, which causes more CO_2 near the walls absorbed.

In order to compare the simulation results with the experimental data, the overall gas phase mass transfer coefficient is introduced, and this is given by (Jassim et al., 2007):

$$K_G a = \frac{Q_G}{\pi({r_o}^2 - {r_i}^2)Z} ln\left(\frac{y_{CO2,in}}{y_{CO2,out}}\right) \quad (49)$$

The CFD simulations examined 18 cases for the CO_2 capture by liquid amine. The simulation results and the validation experimental data are presented in Fig. 9 and $y_{CO2,out}$ is calculated from the average of the CO_2 mass fraction at the gas outlet. For the 30% MEA and the 90% MEA solutions, $K_G a$ is enhanced with increasing the rotation speed and L/G ratio for both the experimental data and the simulations. For the 30% MEA solutions, the simulations predicted $K_G a$ is in the range of 1.7 - 2.0 s^{-1} and the validated experimental data obtained similar results for $K_G a$ between 1.7 s^{-1} and 2.4 s^{-1}. On the other hand, for the 30% MEA, the $K_G a$ values changes only slightly for both the simulations and the experimental data when the L/G ratio increases from 2.8 to 3.7. It is observed that the simulation results are slightly lower than the experimental data, e.g. for the 30% MEA solutions, L/G = 3.3 and n = 850 rpm, $K_G a$ is 2.3 s^{-1} and 1.8 s^{-1} for the experimental data and simulations, respectively, and the simulation result is 21.7% lower than the experimental data.

For the 90% MEA solutions, the results of the $K_G a$ obtained from the experimental data is in the range of 4.6 s^{-1} to 6.1 s^{-1} under all the experimental conditions. As the L/G ratio increases from 0.9 to 1.2, $K_G a$ increases to more than 1.3. For example, at n = 850 rpm, $K_G a$

increases from 4.7 s^{-1} to 5.3 s^{-1} and 6.0 s^{-1} when the L/G ratio increases from 0.8 to 1.0 and 1.2. However, $K_G a$ increases very slightly as the rotation speed increases. For example, at L/G = 3.3, $K_G a$ increases from 5.2 s^{-1} to 5.3 s^{-1} and 5.6 s^{-1} when the rotation speed increases from 600 to 850 and 1150 rpm. $K_G a$, as obtained from the simulations, lies in the range 1.8 s^{-1} to 2.0 s^{-1} for all the simulation cases investigated. The predicted $K_G a$ by the CFD simulation is lower than the experimental data. For the 90% MEA solutions and n = 850 rpm, $K_G a$ is 4.7 s^{-1}, 5.3 s^{-1}, 6.0 s^{-1} for the experimental data, respectively, and 1.8 s^{-1}, 1.9 s^{-1}, 2.0 s^{-1} for the simulations, respectively, for L/G = 0.9, 1.0 and 1.2. The simulation results are 61.7%, 64.2% and 66.7% lower than the experimental results, respectively. The predicted $K_G a$ under the 90% MEA solutions follows the experimental trend that $K_G a$ increases with the increase in the rotation speed and L/G ratio.

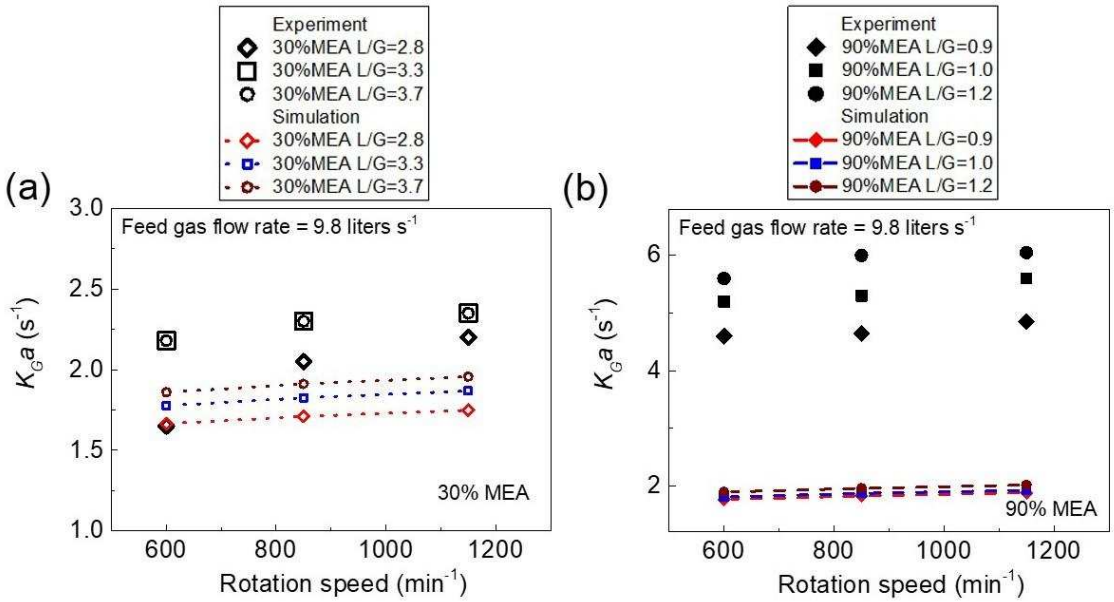

Fig. 9. Comparison of the overall gas phase mass transfer coefficient for the CO_2 absorption into the MEA between the simulations and experimental data, (a) 30% MEA solutions; and (b) 90% MEA solutions.

Fig. 9 shows that the simulated $K_G a$ is lower than the experimental values. In order to more easily resolve this complex problem, we have simplified the model through some assumptions. On the other hand, the experiments were performed in a lab-scale reactor, which may introduce some difficulties and uncertainties for the measurements of the variables, e.g. temperatures and CO_2 concentration inside the reactor. Further, the experimental data for the CO_2 absorptions shown in Fig. 9 was measured at the gas inlet and outlet pipes instead of the inlet and outlet of the packing region. Also the reactions taking place on the surfaces outside the packing, such as on the internal sidewalls of the case, etc. can be significant in particular in the case of the high concentration of the MEA. Here we give a simple estimation. Since the reaction and mass transfer are mainly controlled by the interfacial area, thus we compare the possible extra area outside the packing in the rig for the reaction with the area inside the packing for the reaction. The area outside the packing includes the areas of the front and back sidewalls of the case and the areas of the front and back side plates of the packing, thus the total extra area is 0.24 m^2. Considering the wet fraction outside the packing of 30% which is estimated from the wet fraction inside the packing on 200 m^2/m^3 (average wet area)/663 m^2/m^3 (total area) for the 90% MEA solutions, the real total extra interfacial area for the reaction is 0.072 m^2. For the cases of the 30% and 90% MEA solutions, the predicted interfacial area of the gas and liquid for the reaction inside the packing is 0.39 m^2 (on average 300 m^2/m^3 (wet area per volume) × 0.0013 m^3 (packing volume)) and 0.26 m^2 (on average 200 m^2/m^3 × 0.0013 m^3), respectively. Therefore, there is an 18% area increase to the area inside the packing for the 30% MEA solution and 28% area increase for the 90% MEA solution. For the 30% MEA solution, 18% of the area difference is close to our prediction error of 20% in Fig. 9. For the 90% MEA solution, we consider that there is a noticeable increase in the liquid temperature at the exit of the packing from 313 K to 333 K which results in a 2.8 times higher reaction rate than that at the liquid inlet. Thus for the 90% MEA

solution, 28% of the area increase combined with the 2.8 times higher reaction rate results in approximately 70% increase in the mass transfer rate, which is close to our prediction error of about 60% in Fig. 9. Therefore, we are of the opinion that the discrepancy between the simulation results and experimental data is relatively reasonable and acceptable bearing in mind that only the reactions taking place inside the packing have been calculated in the simulation. In conclusion, the experimental data employed in this work has produced some primary encouraging validations. Our simulations are based on the experimental data from the literature (Lee et al., 2017). In order to verify the explanation by using experimental data, ideally new experiments and in particular a more sophisticated and advanced measurement system need to be developed. For the purpose of demonstrating the potential of employing the approach presented in this paper for the efficient prediction of CO_2 absorption in an RPB, the results from the 2D simulations have given us confidence of the developed model. To improve the comparison with the experiments, new experiments and more advanced measurement technology need to be employed and the full-scale 3D simulations need to be performed in the future. Nevertheless, further improvements of the model are required, such as considering the entrance region and unsteadies of the mass transfer processes in a more detail manner in order to improve the accuracy of the model predictions.

Eq. 49 shows that K_Ga has an index relationship with $y_{CO2,out}$. When $y_{CO2,out}$ becomes smaller, K_Ga increases steeply. Actually, if one considers the error between the simulation and the experiment for the CO_2 mass fraction in the gas phase, the error would be much smaller than that for K_Ga.

The high concentration MEA solutions cause high corrosion to the equipment. In this work, the purpose of the 90% MEA solution used is to investigate the effect of the MEA concentration on the CO_2 absorption in comparison with the low MEA solutions, e.g. the 30% MEA solution. In addition, the Jassim experiments (Jassim et al., 2007) showed that the high

concentration MEA solutions give a higher overall gas phase mass transfer coefficient, $K_G a$, for the CO_2 absorption in the RPB. This work further conforms their result.

Through the validation of the simulation by the liquid holdup distribution and the overall gas phase mass transfer coefficient in the experiments, it is demonstrated that the CFD simulation method proposed in this work is reasonable and effective for the modelling of the multiphase reactions in RPBs.

5.3 Liquid temperature

Fig. 10 shows the liquid temperature contours (Figure 10(a) for 30% MEA and Figure 10(b) for 90% MEA) and distributions for the 30% MEA and the 90% MEA solutions along the bed centerline in the radial direction. In the RPB, the liquid temperature increases from the inner boundary of the packing to the outer boundary of the packing. The highest temperature is T_L = 318.5 K for the 30% MEA solution and T_L = 337.9 K for the 90% MEA solution. The reason that the temperature of the 90% MEA solution is higher than that for the 30% MEA solution is that the 90% MEA solution captures more CO_2 and releases more reaction heat. For the 90% MEA solution, the highest temperature is situated at r = 0.136 m and after r = 0.136 m, the liquid temperature decreases. This is because there is a heat exchange between the fresh air at the temperature of (T = 313.2 K) and hot liquid (T = 337.9 K). The lowest temperature in the reactor appears in the region below the inner boundary of the RPB, and this approaches 313.2 K.

Currently, it is difficult to measure the temperature distribution in the packing of the RPB when it is in operation and we have not found any data in the literature on this issue. Our simulations are based on the experimental data from the literature (Lee et al., 2017), in which there is no data of the temperature in the packing. Since the trend for CO_2 absorption is predicted correctly, this gives us confidence in the temperature prediction. Furthermore, it is

one of the advantages of CFD simulations that it can predict or estimate quantities which are difficult to obtain experimentally.

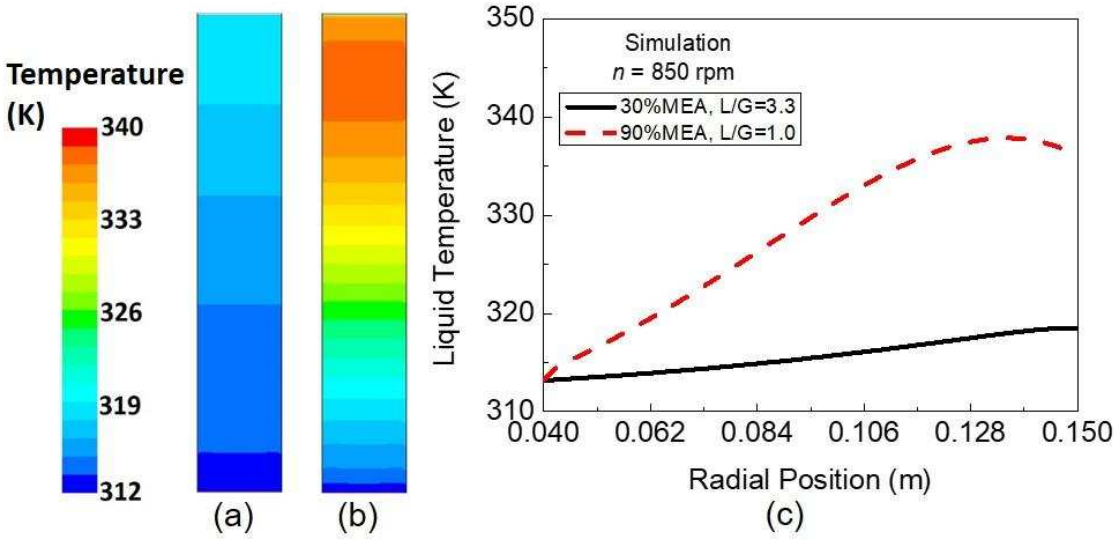

Fig. 10. Contours of the liquid temperature (a) 30% MEA, L/G = 3.3, n = 850 rpm; (b) 90% MEA, L/G = 1.0, n = 850 rpm; and (c) the liquid temperature as a function of the radial position for the different MEA solutions along the bed centreline in the radial direction.

5.4 Gas radial velocity and liquid radial velocity

Fig. 11(a) shows the gas radial velocity of the 30% MEA and the 90% MEA solutions along the bed centreline in the radial direction under the rotation speed of 850 rpm. It indicates that the absolute gas radial velocity increases from the outer boundary to the inner boundary because of the decrease in the cross-sectional area, through which the gas flows. The simulated gas radial velocity for the 30% MEA and 90% MEA basically matches the equation of $U_G = Q_G / (2\pi Zr)$. The slight difference is caused by the absorption of CO_2 by MEA.

The liquid radial velocity is one of the most important characteristics in the gas-liquid two-phase flow in the RPB. Fig. 11(b) shows the liquid radial velocity distribution along the bed centreline. In the RPB, the radial velocity increases along the radial direction. The liquid

radial velocities within the packing region increase slightly from 0.30 m/s to 0.55 m/s for the 30% MEA solution and from 0.14 m/s to 0.29 m/s for the 90% MEA solution. Through a series of simulations, it indicates that the rotation speed influences the liquid radial velocity highly and with the increase of the rotation speed, the liquid radial velocity increases correspondingly.

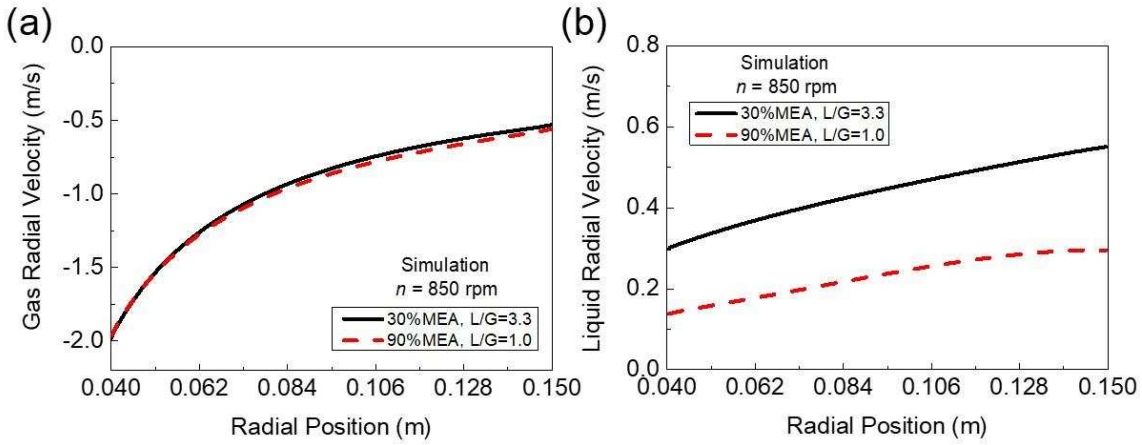

Fig. 11. Gas radial velocity (a) and liquid radial velocity (b) along the radial direction for the 30% MEA, L/G = 3.3, n = 850 rpm and the 90% MEA, L/G = 1.0, n = 850 rpm.

5.5 Pressure distribution

Fig. 12 shows the pressure distributions of the 30% MEA and 90% MEA solutions along the bed centreline in the radial direction. In the whole reactor, the pressure decreases from the gas inlet to the gas outlet. In the packing region, the pressure near the inner boundary has a non-linear relationship with the radial position, except that the pressure is a linear function of the radial positon in the packing region. For the 30% MEA solution, the pressure drop in the packing is 232.6 Pa. For the 90% MEA solution, the pressure drop in the packing is 235.4 Pa, which is slightly higher than that for the 30% MEA solution. This is because the 90% MEA solution has higher viscosity and thus causes higher flow resistance and pressure.

In the experiment, the pressure has not been measured but we can compare the simulation results to similar experimental data that is available in the literatures. For the Hassan-Beck experiment (1997), the packed bed has an inner diameter of 79 mm, the outer diameter of 201 mm, and the thickness of 60 mm; the porosity of the packing is 0.83 and the specific area of the packing is 1428 m^2/m^3. Under Q_L = 10.5 L/min or 14.4 L/min, Q_G = 50 - 70 m^3/h and n = 620 rpm, the pressure drop is 20 - 50 mmH_2O (196 Pa - 490 Pa). In our simulations, the operating conditions and facilities are similar to the above experimental conditions and we find the pressure drop is 200 Pa - 250 Pa, which is in the range of 196 Pa - 490 Pa. Thus, we may conclude that the predicted pressure is reasonable.

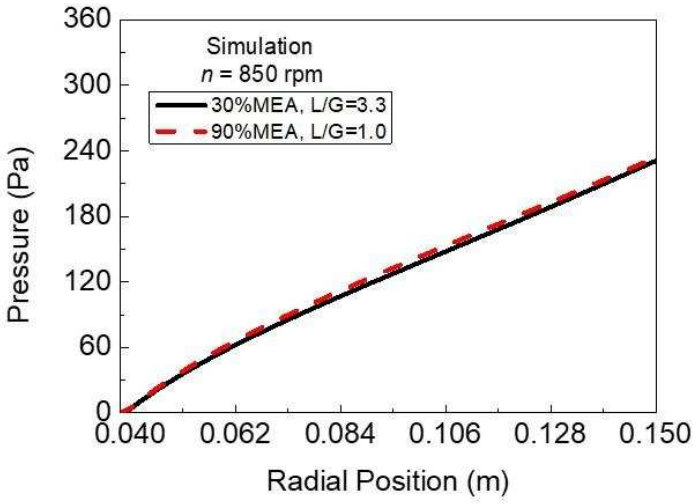

Fig. 12. Pressure distribution along the radial direction for the 30% MEA, L/G = 3.3, n = 850 rpm and the 90% MEA, L/G = 1.0, n = 850 rpm.

6. Conclusions

In this paper, the CO_2 absorption by the liquid amine in the RPB has been, for the first time, successfully simulated by the Eulerian-Eulerian CFD method. A new gas-liquid two-phase porous media model, based on the Kołodziej one phase model, is employed in order to

describe the flow resistance. The liquid generation zone and the liquid elimination zone were constructed and their corresponding models were built for setting the gas-liquid counter-current flow. The combination of these new models is validated by the Burns experimental correlation and they are demonstrated to be robust in predicting the liquid holdup distribution in RPBs. The model for the interfacial area between the gas and liquid is derived from the VOF simulation of the liquid flow on real wire screens.

The 18 cases investigated for the CO_2 absorption using MEA solutions in the RPB were simulated and validated with the available experimental data. For the 30% MEA solutions, the L/G ratio is 2.8, 3.3 or 3.7 and the rotation speed is 600, 850 or 1150 rpm, whereas for the 90% MEA solutions, the L/G ratio is 0.9, 1.1 or 1.2 and the rotation speed is 600, 850 or 1150 rpm. Finally, the results were analysed and discussed.

In conclusion, this work provides an effective CFD method to model multiphase reactions in RPBs and this method is feasible for scaling up investigations on the simulation of large-scale RPBs.

Acknowledgements

The authors would like to acknowledge the financial support provided by the Engineering and Physical Science Research Council (EPSRC) under grant EP/M001458/2. In addition, P. Xie would like to acknowledge the China Scholarship Council and the University of Sheffield for funding his research studies.

Nomenclature

A_{GL}	interfacial area, m^2
a_R	correction coefficient

a_S	specific area of the packing materials, $m^2 \cdot m^{-3}$
a'_S	specific area of the wet wires, $m^2\ m^{-3}$
C	concentration, $kmol \cdot m^{-3}$
D	diffusivity, $m^2 \cdot s^{-1}$
D_h	hydraulic diameter, m
d_p	equivalent sphere diameter of the packing materials, m
d_w	wire diameter, m
d'_w	wire and liquid film diameter, m
E	total energy, activation energy, J
E_x	enhancement factor
F_{GL}	drag force between the gas and liquid, $N\ m^{-3}$
f	friction factor
f_{app}	Fanning friction factor for developing laminar flow
f_e	ratio of wetted packing or ratio of interfacial area to the total packing surface area
f_t	Fanning friction factor for developing turbulence flow
g	acceleration due to gravity, $m \cdot s^{-2}$
g_c	centrifugal acceleration, $m \cdot s^{-2}$
g_0	characteristic centrifugal acceleration (=100 $m \cdot s^{-2}$), $m \cdot s^{-2}$
g_1	characteristic centrifugal acceleration (=205.6 $m \cdot s^{-2}$), $m \cdot s^{-2}$
H	Henry constant, $m^3 \cdot Pa \cdot mol^{-1}$
H_L	enthalpy of the liquid phase, $J \cdot mol^{-1}$
h	enthalpy of species, $J \cdot mol^{-1}$
h_{GL}	heat transfer coefficient, $W \cdot m^{-2} \cdot K^{-1}$
h_L	liquid holdup
J	diffusion flux of species, $kg \cdot m^{-2} \cdot s^{-1}$
K_Ga	overall gas phase mass transfer coefficient, $m \cdot s^{-1}$
k_b	reaction rate constant, $m^6 \cdot kmol^{-2} \cdot s^{-1}$
k_{eff}	effective conductivity, $W \cdot m^{-1} \cdot K^{-1}$
k_{GL}	total mass transfer coefficient between gas and liquid, $m \cdot s^{-1}$
k_L*	mass transfer coefficient in the liquid phase from film theory , $m \cdot s^{-1}$
k_i	mass transfer coefficient in the i phase, $m \cdot s^{-1}$

k_1	reaction rate constant, $m^3 \cdot kmol^{-1} \cdot s^{-1}$
k_2	reaction rate constant, $m^3 \cdot kmol^{-1} \cdot s^{-1}$
L	liquid mass flux, $kg \cdot m^{-2} \cdot s^{-1}$
Mw	molar mass, $g \cdot mol^{-1}$
$m_{GL,CO2}$	CO_2 mass transfer between the gas and liquid, $kg \cdot s^{-1}$
n	rotation speed, rpm
P	pressure, Pa
$Q_{h,GL}$	transferred heat between the gas phase and liquid phase, W
Q_i	volume flow rate, $m^3 \cdot s^{-1}$
R	gas constant, 8.314 $J \cdot mol^{-1} \cdot K^{-1}$
R_j	net rate of production of the j species by chemical reactions
r	radial coordinate, m
r_i	inner radius of the rotating packed bed, m
r_o	outer radius of the rotation packed bed, m
Δr	radial separation, m
r_{CO2}	CO_2 reaction rate
S_i	momentum source, $kg \cdot m \cdot s^{-2}$
S_{LS}	interaction force between the liquid and solids of the packing materials, N
S_{GS}	interaction force between gas and solids of packing materials, N
$S_{m,i}$	mass source, $kg \cdot m^{-3} \cdot s^{-1}$
T_i	temperature of the i phase, K
U	liquid flow rate per unit area or superficial velocity, $m \cdot s^{-1}$
U_0	characteristic flow rate per unit area (=1 $cm \cdot s^{-1}$), $m \cdot s^{-1}$
U_1	characteristic flow rate per unit area (=0.0106 $m \cdot s^{-1}$), $m \cdot s^{-1}$
V	volume, m^3
v	velocity, $m \cdot s^{-1}$
v_e	effective velocity, $m \cdot s^{-1}$
x	axial coordinate, m
Δx	axial separation, m
Y	mass fraction of each species
$y_{CO2,in}$	molar fraction of CO_2 in the gas inlet to the rotating packed bed

$y_{CO2,out}$	molar fraction of CO_2 in the gas outlet from the rotating packed bed
Z	width or axial length of the rotating packed bed, m
z	tangential coordinate, m

Greek

α_i	phase fraction
χ^+	dimensionless channel length
δ_{sim}	error for simulation
ε	porosity of packed bed
ε_i	volume fraction of the i phase
γ	dynamic contact angle, °
γ_1	characteristic dynamic contact angle (= 75°), °
ℓ	diffusion layer thickness for mass transfer, m
κ	thermal conductivity, $W \cdot m^{-1} \cdot K^{-1}$
$\mu_{0.3}$	dynamic viscosity for the 30 wt% MEA solution, mPa·s
$\mu_{0.9}$	dynamic viscosity for the 90 wt% MEA solution, mPa·s
μ_i	dynamic viscosity of the i phase, Pa·s
ν	kinematic viscosity, $m^2 \cdot s^{-1}$
ν_0	characteristic kinematic viscosity (= 1.0×10^{-6} $m^2 \cdot s^{-1}$), $m^2 \cdot s^{-1}$
ν_1	characteristic kinematic viscosity (= 3.35×10^{-6} $m^2 \cdot s^{-1}$), $m^2 \cdot s^{-1}$
θ	angle of flow direction slop to the bed axis, °
ρ_i	density of the i phase, $kg \cdot m^{-3}$
$\rho_{L,CO2}^*$	CO_2 concentration on the surface of the liquid flow, $kg \cdot m^{-3}$
$\rho_{L,CO2}$	CO_2 concentration in the liquid bulk flow, $kg \cdot m^{-3}$
τ	bed tortuosity factor
ω	rotation speed, $rad \cdot s^{-1}$

Dimensionless parameters

Ha	Hatta number

Nu	Nusselt number
Pr	Prandtl number
Re	Reynold number

Subscripts

CO2	carbon dioxide
exp	experiment
G	gas phase
i	= G, L
j	j coordination (axial, radial or tangential coordinate)
k	k species
L	liquid phase
MEA	monoethanolamine
r	radial coordinate
reactor	reactor rig
S	solids phase for the packing materials
sim	simulation
w	wall
x	axial coordinate
z	tangential coordinate

References

Aboudheir, A., Tontiwachwuthikul, P., Chakma, A., Idem, R., 2003. Kinetics of the reactive absorption of carbon dioxide in high CO_2-loaded, concentrated aqueous monoethanolamine solutions. Chem. Eng. Sci. 58, 5195-5210.

Amundsen, T.G., Øi, L.E., Eimer, D.A., 2009. Density and viscosity of monoethanolamine + water + carbon dioxide from (25 to 80) °C. J. Chem. Eng. Data. 54, 3096-3100.

Asendrych, D., Niegodajew, P., Drobniak, S., 2013. CFD modelling of CO_2 capture in a packed bed by chemical absorption. Chem. Process. Eng. 34, 269-282.

Attou, A., Boyer, C., Ferschneider, G., 1999. Modelling of the hydrodynamics of the concurrent gas-liquid trickle flow through a trickle-bed reactor. Chem. Eng. Sci. 54, 785-802.

Burns, J.R., Jamil, J.N., Ramshaw, C., 2000. Process intensification: operating characteristics of rotating packed beds-determination of liquid hold-up for a high voidage structured packing. Chem. Eng. Sci. 55, 2401-2415.

Chen, Y.-S., Lin, C.-C., Liu, H.-S., 2005a. Mass transfer in a rotating packed bed with viscous Newtonian and non-Newtonian fluids. Ind. Eng. Chem. Res. 44, 1043-1051.

Chen, Y.-S., Lin, C.-C., Liu, H.-S., 2005b. Mass transfer in a rotating packed bed with various radii of the bed. Ind. Eng. Chem. Res. 44, 7868-7875.

Chen, Y.-S., Lin, F.-Y., Lin, C.-C., Tai, C.Y.-D., Liu, H.-S., 2006. Packing characteristics for mass transfer in a rotating packed bed, Ind. Eng. Chem. Res. 45, 6846-6853.

Fitzgerald, F.D., Hume, S.A., McGough, G., Damen, K., 2014. Ferrybridge CCPilot 100+ operating experience and final test results. Energy Procedia. 63, 6239-6251.

Fluent, Ansys Fluent theory guide, Ansys Inc, 2013.

Guo, F., Zheng, C., Guo, K., Feng, Y., Gardner, N.C., 1997. Hydrodynamics and mass transfer in cross-flow rotating packed bed, Chem. Eng. Sci. 52, 3853-3859.

Guo, T.Y., Shi, X., Chu, G.W., Xiang, Y., Wen, L.X., Chen, J.F., 2016. Computational fluid dynamics analysis of the micromixing efficiency in a rotating-packed-bed reactor. Ind. Eng. Chem. Res. 55, 4856-4866.

Guo, T.Y., Cheng, K.P., Wen, L.X., Andersson, R., Chen, J.F., 2017. Three-dimensional simulation on liquid flow in a rotating packed bed reactor. Ind. Eng. Chem. Res. 56, 8169-8179.

Halmann, M.M., Stenberg, M., 1999. Greenhouse Gas Carbon Dioxide Mitigation. CRC Press LLC: Boca Raton, FL.

Hassan-Beck, H.M., 1997. Process intensification: mass transfer and pressure drop for counter current rotating packed beds. PhD dissertation, University of Newcastle-upon-Tyne.

Hikita, H., Asai, S., Ishikawa, H., Honda, M., 1977. The kinetics of reactions of carbon dioxide with monoethanolamine, diethanolamine and triethanolamine by a rapid mixing method, Chem. Eng. J. 13, 7-12.

Hlushkou, D., Tallarek, U., 2006. Transition from creeping via viscous-inertial to turbulent, J. Chromatography A, 1126, 70-85.

Horng, S.Y., Li, M.H., 2002. Kinetics of absorption of carbon dioxide into aqueous solutions of Monoethanolamine + Triethanolamine. Ind. Eng. Chem. Res. 41, 257-266.

Hosseini, S.M., Alizadeh, R., Fatehifar, E., Alizahehdakhel, A., 2014. Simulation of gas absorption into string-of-beads liquid flow with chemical reaction. Heat Mass Transfer. 50, 1393-1403.

Hughmark, G.A., 1967. Mass and heat transfer from rigid spheres, AIChE J. 13, 1219-1221.

Iliuta, I., Petre, C.F., Larachi, F., 2004. Hydrodynamic continuum model for two-phase flow structured-packing-containing columns. Chem. Eng. Sci. 59, 879-888.

International Energy Agency, 2017. Electricity information: Overview.

Iso, Y., Huang, J., Kato, M., Matsuno, S., Takano, K., 2013. Numerical and experimental study on liquid film flows on packing elements in absorbers for post-combustion CO_2 capture. Energy Procedia. 37, 860-868.

Jassim, M.S., Rochelle, G., Eimer, D., Ramshaw, C., 2007. Carbon dioxide absorption and desorption in aqueous monoethanolamine solutions in a rotating packed bed. Ind. Eng. Chem. Res. 46, 2823-2833.

Jeannot M.A., Cantwell, F.F., 1997. Mass transfer characteristics of solvent extraction into a single drop at the tip of a syringe needle, Anal. Chem. 69, 235-239.

Joel, A.S., Wang, M., Ramshaw, C., Oko, E., 2017. Modelling, simulation and analysis of intensified regenerator for solvent based carbon capture using rotating packed bed technology. Appl. Energy. 203, 11-25.

Kang, J.L., Sun, K., Wong, D.S.H., Jang, S.S., Tan, C.S., 2014. Modelling studies on absorption of CO_2 by monoethanolamine in rotating packed bed. Int. J. Greenhouse Gas Control. 25, 141-150.

Kang, J.L., Wong, D.S.H., Jang, S.S., Tan, C.S., 2016. A comparison between packed beds and rotating packed beds for CO_2 capture using monoethanolamine and dilute aqueous ammonia solutions. Int. J. Greenhouse Gas Control. 46, 228-239.

Kim, J., Pham, D.A., Lim, Y., 2016. Gas-liquid multiphase computational fluid dynamics (CFD) of amine absorption column with structured-packing for CO_2 capture. Comput. Chem. Eng. 88, 39-49.

Kołodziej, A., Łojewska, J., 2009. Experimental and modelling study on flow resistance of wire gauzes. Chem. Eng. Process. 48, 816-822.

Lappalainen, K., Alopaeus, V., Manninen, M., Aittamaa, J., 2008. Improved hydrodynamic model for wetting efficiency, pressure drop, and liquid holdup in trickle-bed reactors. Ind. Eng. Chem. Res. 47, 8436-8444.

Lee, J., Kolawole, T., Attidekou, P., 2017. Carbon capture from a simulated flue gas using a rotating packed bed adsorber and mono ethanol amine (MEA). Energy Procedia. 114, 1834-1840.

Levich, V.G., 1962. Physicochemical hydrodynamics, Prentice-Hall, Englewood Cliffs, N.J.

Liu, G.B., Yu, K.T., Yuan, X.G., Liu, C.J., 2006a. New model for turbulent mass transfer and its application to the simulations of a pilot-scale randomly packed column for CO_2-NaOH chemical absorption. Ind. Eng. Chem. Res. 45, 3220-3229.

Liu, G.B., Yu, K.T., Yuan, X.G., Liu, C.J., Guo, Q.C., 2006b. Simulation of chemical absorption in pilot-scale and industrial-scale packed columns by computational mass transfer. Chem. Eng. Sci. 61, 6511-6529.

Liu, H.-S., Lin, C.-C., Wu, S.-C., Hsu, H.-W., 1996. Characteristics of a rotating packed bed, Ind. Eng. Chem. Res. 35, 3590-3596.

Lu, X., Holland, D.J., 2016. Investigation of drag models for the two fluid simulation of Geldart group A powders. Powder Technol. 304, 41-54.

Lu, X., Xie, P., Ingham, D.B., Ma, L., Pourkashanian, M., 2018. A porous media model for CFD simulations of gas-liquid two-phase flow in rotating packed beds. Chem. Eng. Sci. 189, 123-134.

Luo, Y., Chu, G.-W., Zou, H.-K., Zhao, Z.-Q., Dudukovic, M.P., Chen, J.-F., 2012. Gas-liquid effective interfacial area in a rotating packed bed, Ind. Eng. Chem. Res. 51, 16320-16325.

Ma, C., Pietrucci, F., Andreoni, W., 2015. Capture and release of CO_2 in monoethanolamine aqueous solutions: new insights from first-principles reaction dynamics. J. Chem. Theory Comput. 11, 3189-3198.

Mansourizadeh, A., Ismail, A.F., 2009. Hollow fibre gas-liquid membrane contactors for acid gas capture: A review. J. Hazard. Mater. 171, 38-53.

Martínez, E., Jaimes, R., Gomez, J.L., Filho, R.M., 2012. CFD simulation of three-dimensional multiphase flow in a rotating packed bed. Comput. Aided Chem. Eng. 30, 1158-1162.

Mishra, D.P., 2014. Simulation of carbon dioxide-monoethanolamine-water system using equilibrium approach. Thesis. Department of Chemical Engineering, National Institute of Technology (India).

Mooney, K.G., Mintun, M.A., Himmelstein K.J., Stella, V.J., 1981. Dissolution kinetics of carboxylic acids I: Effect of pH under unbuffered conditions, J. Pharm. Sci. 70, 13-22.

Munjal, S., Dudukovic, M.P., Ramachandran, P., 1989a. Mass-transfer in rotating packed packed beds-I. Development of gas-liquid and liquid solid mass-transfer correlations, Chem. Eng. Sci. 44, 2245-2256.

Munjal, S., Dudukovic, M.P., Ramachandran, P., 1989b. Mass-transfer in rotating packed beds-II. Experimental results and comparison with theory and gravity flow, Chem. Eng. Sci. 44, 2257-2268.

Niegodajew, P., Asendrych, D., 2016. Amine based CO_2 capture-CFD simulation of absorber performance. Appl. Math. Modell. 40, 10222-10237.

Øi, L.E., 2010. CO_2 removal by absorption: challenges in modelling. Math. Comput. Modell. Dyn. Syst. 16, 511-533.

Oko, E., Wang, M., Joel, A.S., 2017. Current status and future development of solvent-based carbon capture. Int. J. Coal Sci. Technol. 4, 5-14.

Onda, K., Takeuchi, H., Okumoto, Y., 1968. Mass transfer coefficients between gas and liquid phases in packed columns. J. Chem. Eng. Jpn. 1, 56-62.

Penttilä, A., Dell'Era, C., Uusi-Kyyny, P., Alopaeus, V., 2011. The Henry's law constant of N_2O and CO_2 in aqueous binary and ternary amine solutions (MEA, DEA, DIPA, MDEA and AMP). Fluid phase Equilib. 311, 59-66.

Pham, D.A., Lim, Y., Jee, H., Ahn, E., Jung, Y., 2015. Porous media Eulerian computational fluid dynamics (CFD) model of amine absorber with structured-packing for CO_2 removal. Chem. Eng. Sci. 132, 259-270.

Plaza, J.M., Wagener, D.V., Rochelle, G.T., 2010. Modelling CO_2 capture with aqueous monoethanolamine, Int. J. Greenhouse Gas Control. 4, 161-166.

Rajan, S., Kumar, M., Ansari, M.J., Rao, D.P., Kaistha, N., 2011. Limiting gas liquid flows and mass transfer in a novel rotating packed bed (HiGee), Ind. Eng. Chem. Res. 50, 986-997.

Raynal, L., Royon-Lebeaud, A., 2007. A multi-scale approach for CFD calculations of gas-liquid flow within large size column equipped with structured packing. Chem. Eng. Sci. 62, 7196-7204.

Raynal, L., Rayana, F.B., Royon-Lebeaud, A., 2009. Use of CFD for CO_2 absorbers optimum design: from local scale to large industrial scale. Energy Procedia. 1, 917-924.

Saskpower, 2018. http://www.saskpower.com/our-power-future /carbon-capture-and-storage /boundary-dam-carbon-capture-project/

Sebastia-Saez, D., Gu, S., Ranganathan, P., 2014. Volume of fluid modelling of the reactive mass transfer of CO_2 into aqueous amine solutions in structured packed elements at micro-scale. Energy Procedia. 63, 1229-1242.

Sebastia-Saez, D., Gu, S., Ranganathan, P., Papadikis, K., 2015. Micro-scale CFD modelling of reactive mass transfer in falling liquid films within structured packing materials. Int. J. Greenhouse Gas Control. 33, 40-50.

Sebastia-Saez, D., Gu, S., Ramaioli, M., 2018. Effect of the contact angle on the morphology, residence time distribution and mass transfer into liquid rivulets: A CFD study. Chem. Eng. Sci. 176, 356-366.

Shearer, C., Fofrich, R., Davis, S.J., 2017. Future CO_2 emissions and electricity generation from proposed coal-fired power plants in India. Earth's future. 5, 408-416.

Shi, X., Xiang, Y., Wen, L.X., Chen, J.F., 2013. CFD analysis of liquid phase flow in a rotating packed bed reactor. Chem. Eng. J. 228, 1040-1049.

Snijder, E.D., te Riele, M.J.M., Versteeg, G.F., van Swaaij, W.P.M., 1993. Diffusion coefficients of several aqueous alkanolamine solutions. J. Chem. Eng. Data 38, 475-480.

Tan, C.-S., Chen, J.-E., 2006. Absorption of carbon dioxide with piperazine and its mixtures in a rotating packed bed, Separ. Purif. Technol. 49, 174-180.

Tomiyama, A., 1998. Struggle with computational bubble dynamics. 3rdThird International Conference on Multiphase Flow, Lyon, France.

Tung, H.H., Mah, R.S.H., 1983. Modeling liquid mass transfer in Higee separation process, Chem. Eng. Commum. 39, 147-153.

U.S. Energy Information Administration, 2017. Electric power monthly with data for September 2017. U.S. Department of Energy, Washington, DC 20585.

Versteeg, G.F., van Dijck, L.A.J., van Swaaij, W.P.M., 1996. On the kinetics between CO_2 and alkanolamines both in aqueous and non-aqueous solutions: an overview, Chem. Eng. Commun. 144, 113-158.

Wang, M., Joel, A.S., Ramshaw, C., Eimer, D., Musa, N.M., 2015. Process intensification for post-combustion CO_2 capture with chemical absorption: A critical Review. Appl. Energy. 158, 275-291.

Wang, Z., Fang, M., Yu, H., Ma, Q., Luo, Z., 2013. Modelling of CO_2 stripping in a hollow fibre membrane contactor for CO_2 capture. Energy Fuel. 27, 6887-6898.

Wegner, K., 2017. Theories for mass transfer coefficients. PPT of Lecture. Swiss Federal Institute of Technology.

Wellek, R.M., Brunson, R.J., Law, F.H., 1978. Enhancement factors for gas-absorption with second-order irreversible chemical reaction. Can. J. Chem. Eng. 56, 181-186.

Xie, P., Lu, X., Yang, X., Ingham, D., Ma, L., Pourkashanian, M., 2017. Characteristics of liquid flow in a rotating packed bed for CO_2 capture: A CFD analysis. Chem. Eng. Sci. 172, 216-229.

Xie, P., Lu, X., Ding, H., Yang, X., Ingham, D., Ma, L., Pourkashanian, M., 2018. A mesoscale 3D CFD analysis of the liquid flow in a rotating packed bed. Chem. Eng. Sci. submitted.

Yang, W., Wang, Y., Chen, J., Fei, W., 2010. Computational fluid dynamic simulation of fluid flow in a rotating packed bed. Chem. Eng. J. 156, 582-587.

Yang, Y., Xiang, Y., Chu, G., Zou, H., Luo, Y., Arowo, M., Chen, J., 2015. A noninvasive X-ray technique for determination of liquid holdup in a rotating packed bed. Chem. Eng. Sci. 138, 244-255.

Yang, Y., Xiang, Y., Chu, G., Zou, H., Sun, B., Arowo, M., Chen, J., 2016. CFD modelling of gas-liquid mass transfer process in a rotating packed bed. Chem. Eng. J. 294, 111-121.

Zhao, B., Su, Y., Tao, W., 2014. Mass transfer performance of CO_2 capture in rotating packed bed: dimensionless modelling and intelligent prediction, Appl. Energy. 136, 132-142.

Zhao, B., Tao, W., Zhong, M., Su, Y., Cui, G., 2016. Process, performance and modelling of CO_2 capture by chemical absorption using high gravity: A review. Renewable and Sustainable Energy Rev. 65, 44-56.